The Astrophysical Journal Letters, 984:L18 (16pp), 2025 May 1 https://doi.org/10.3847/2041-8213/adc430

exoALMA. XIII. Gas Masses from N_2H^+ and $C^{18}O$: A Comparison of Measurement Techniques for Protoplanetary Gas Disk Masses

Leon Trapman[1], Cristiano Longarini[2,3], Giovanni P. Rosotti[3], Sean M. Andrews[4], Jaehan Bae[5], Marcelo Barraza-Alfaro[6], Myriam Benisty[7,8,9], Gianni Cataldi[10], Pietro Curone[3,11], Ian Czekala[12,13], Stefano Facchini[3], Daniele Fasano[8,7], Mario Flock[9], Misato Fukagawa[10], Maria Galloway-Sprietsma[5], Himanshi Garg[14], Cassandra Hall[15,16,17], Jane Huang[18], John D. Ilee[19], Andres F. Izquierdo[5,20,21,31], Kazuhiro Kanagawa[22], Geoffroy Lesur[7], Giuseppe Lodato[3], Ryan A. Loomis[23], Ryuta Orihara[22], Teresa Paneque-Carreno[24,32], Christophe Pinte[7,14], Daniel Price[14], Jochen Stadler[7,8], Richard Teague[6], Sierk van Terwisga[25], Leonardo Testi[26,27], Hsi-Wei Yen[28], Gaylor Wafflard-Fernandez[7], David J. Wilner[4], Andrew J. Winter[8,9], Lisa Wölfer[6], Tomohiro C. Yoshida[10,29], Brianna Zawadzki[30], and Ke Zhang[1]
[1] Department of Astronomy, University of Wisconsin-Madison, 475 N Charter St, Madison, WI 53706, USA; ltrapman@wisc.edu
[2] Institute of Astronomy, University of Cambridge, Madingley Road, Cambridge CB3 0HA, UK
[3] Dipartimento di Fisica, Università degli Studi di Milano, Via Celoria 16, I-20133 Milano, Italy
[4] Center for Astrophysics — Harvard & Smithsonian, Cambridge, MA 02138, USA
[5] Department of Astronomy, University of Florida, Gainesville, FL 32611, USA
[6] Department of Earth, Atmospheric, and Planetary Sciences, Massachusetts Institute of Technology, Cambridge, MA 02139, USA
[7] Université Grenoble Alpes, CNRS, IPAG, 38000 Grenoble, France
[8] Université Côte d'Azur, Observatoire de la Côte d'Azur, CNRS, Laboratoire Lagrange, France
[9] Max-Planck Institute for Astronomy (MPIA), Königstuhl 17, 69117 Heidelberg, Germany
[10] National Astronomical Observatory of Japan, 2-21-1 Osawa, Mitaka, Tokyo 181-8588, Japan
[11] Departamento de Astronomía, Universidad de Chile, Camino El Observatorio 1515, Las Condes, Santiago, Chile
[12] School of Physics & Astronomy, University of St. Andrews, North Haugh, St. Andrews KY16 9SS, UK
[13] Centre for Exoplanet Science, University of St. Andrews, North Haugh, St. Andrews KY16 9SS, UK
[14] School of Physics and Astronomy, Monash University, VIC 3800, Australia
[15] Department of Physics and Astronomy, The University of Georgia, Athens, GA 30602, USA
[16] Center for Simulational Physics, The University of Georgia, Athens, GA 30602, USA
[17] Institute for Artificial Intelligence, The University of Georgia, Athens, GA 30602, USA
[18] Department of Astronomy, Columbia University, 538 W. 120th Street, Pupin Hall, New York, NY 10027, USA
[19] School of Physics and Astronomy, University of Leeds, Leeds LS2 9JT, UK
[20] Leiden Observatory, Leiden University, P.O. Box 9513, NL-2300 RA Leiden, The Netherlands
[21] European Southern Observatory, Karl-Schwarzschild-Str. 2, D-85748 Garching bei München, Germany
[22] College of Science, Ibaraki University, 2-1-1 Bunkyo, Mito, Ibaraki 310-8512, Japan
[23] National Radio Astronomy Observatory, Charlottesville, VA 22903, USA
[24] Department of Astronomy, University of Michigan, 1085 South University Avenue, Ann Arbor, MI 48109, USA
[25] Space Research Institute, Austrian Academy of Sciences, Schmiedlstr. 6, A-8042, Graz, Austria
[26] Alma Mater Studiorum Universitá di Bologna, Dipartimento di Fisica e Astronomia (DIFA), Via Gobetti 93/2, 40129 Bologna, Italy
[27] INAF-Osservatorio Astrofisico di Arcetri, Largo E. Fermi 5, 50125 Firenze, Italy
[28] Academia Sinica Institute of Astronomy & Astrophysics, 11F of Astronomy-Mathematics Building, AS/NTU, No.1, Sec. 4, Roosevelt Rd, Taipei 10617, Taiwan
[29] Department of Astronomical Science, The Graduate University for Advanced Studies, SOKENDAI, 2-21-1 Osawa, Mitaka, Tokyo 45181-8588, Japan
[30] Department of Astronomy, Van Vleck Observatory, Wesleyan University, 96 Foss Hill Drive, Middletown, CT 06459, USA
Received 2024 November 29; revised 2025 February 24; accepted 2025 March 6; published 2025 April 28

Abstract

The gas masses of protoplanetary disks are important but elusive quantities. In this work we present new Atacama Large Millimeter/submillimeter Array (ALMA) observations of N_2H^+ (3–2) for 11 exoALMA disks. N_2H^+ is a molecule sensitive to CO freeze-out and has recently been shown to significantly improve the accuracy of gas masses estimated from CO line emission. We combine these new observations with archival N_2H^+ and CO isotopologue observations to measure gas masses for 19 disks, predominantly from the exoALMA large program. For 15 of these disks the gas mass has also been measured using gas rotation curves. We show that the CO + N_2H^+ line emission-based gas masses typically agree with the kinematically measured ones within a factor of 3 ($\sim 1\sigma$–2σ). Gas disk masses from CO + N_2H^+ are on average a factor of $2.3^{+0.7}_{-1.0}\times$ lower than the kinematic disk masses, which could suggest slightly lower N_2 abundances and/or lower midplane ionization rates than typically assumed. Herbig disks are found to have CO gas abundances at the level of the interstellar medium based on their CO and N_2H^+ fluxes, which sets them apart from T Tauri disks, where abundances are typically $\sim 3-30\times$ lower. The agreement between CO + N_2H^+-based and kinematically measured gas masses is promising and shows that multimolecule line fluxes are a robust tool to accurately measure disk masses at least for extended disks.

[31] NASA Hubble Fellowship Program Sagan Fellow.
[32] 51 Pegasi b Fellow.

Unified Astronomy Thesaurus concepts: Protoplanetary disks (1300); Astrochemistry (75); Interferometry (808); Radio interferometry (1346)

1. Introduction

The gas masses of protoplanetary disks are crucial information for planet formation (e.g., A. Morbidelli & S. N. Raymond 2016). The total mass determines whether, and how many, gas giants can be formed in the disk. Furthermore, the gas density plays a large role in the dust physics occurring in the disk, such as grain growth and inward drift rates (e.g., T. Birnstiel 2024; J. Drażkowska et al. 2023). The gas surface density also dictates the migration of planets that have already formed (e.g., S. Paardekooper et al. 2023).

Measuring the gas mass has been plagued with difficulties (see reviews by E. A. Bergin & J. P. Williams 2018; A. Miotello et al. 2023; K. I. Öberg et al. 2023), mainly because H_2, the dominant component of the gas, does not significantly emit at the ∼20–30 K temperature of the bulk of gas mass in protoplanetary disks (e.g., W. F. Thi et al. 2001; A. Carmona et al. 2011; I. Pascucci et al. 2013; C. Pinte et al. 2018; C. J. Law et al. 2021, 2022; T. Paneque-Carreño et al. 2023).

The gas mass therefore has to be measured indirectly. This is most commonly done from the millimeter dust continuum emission, where the observed flux is converted into a dust mass by assuming a dust opacity, an average disk temperature, and that the emission is optically thin (e.g., S. V. W. Beckwith et al. 1990; J. P. Williams et al. 2005; M. Ansdell et al. 2016; C. F. Manara et al. 2023). This dust mass is then converted to a gas mass by assuming a gas-to-dust mass ratio, most commonly using the typical interstellar medium (ISM) value of 100. While this is perhaps the most straightforward way to estimate the disk mass, the dust properties that set the opacity and the gas-to-dust mass ratio are likely different for each disk. Furthermore, there is increasing evidence that some or all of the disk continuum emission is optically thick at wavelengths $\lesssim$1.3 mm (e.g., S. M. Andrews et al. 2018a; M. Tazzari et al. 2021).

The gas mass can also be inferred from less abundant species in the gas. Among these, hydrogen deuteride (HD) is perhaps the most promising because of its close chemical similarities to H_2 (e.g., L. Trapman et al. 2017; J. K. Calahan et al. 2021). Herschel detected HD $J = 1$–0 (112 μm) emission toward three disks, which allowed for robust measurements of gas disk mass (e.g., E. A. Bergin et al. 2013; M. K. McClure et al. 2016; J. K. Calahan et al. 2021; K. R. Schwarz et al. 2021; L. Trapman et al. 2022b), but with the end of the Herschel mission we currently lack a far-infrared observatory capable of observing HD in more disks.

The most commonly used gas mass tracer is therefore CO, the second most abundant molecule in the gas, whose bright millimeter lines are detected toward most protoplanetary disks (e.g., A. Dutrey et al. 1996; W. R. F. Dent et al. 2005; J. P. Williams & W. M. J. Best 2014; M. Ansdell et al. 2016, 2018; F. Long et al. 2017). Initial gas mass measurements based on the optically thin isotopologues of CO, ^{13}CO and C^{18}O, revealed gas-to-dust mass ratios that were much lower than the ISM value (e.g., J. P. Williams & W. M. J. Best 2014; A. Miotello et al. 2017; F. Long et al. 2017). Cross-comparisons with independent gas mass tracers, such as HD, suggested that these CO-based gas masses were underestimating the true disk mass.

The likely cause of this underestimation is the omission of one or more processes affecting gaseous CO in disks (e.g., A. Miotello et al. 2023). The original thermochemical models used to derive gas masses included (isotope-selective) photodissociation and freeze-out, the two dominant processes that set the CO abundance structure (e.g., Y. Aikawa et al. 2002; R. Visser et al. 2009; A. Miotello et al. 2014; M. Ruaud & U. Gorti 2019). Several processes have been suggested to explain the low CO-based gas masses, including the chemical conversion of CO into more complex, less volatile species (e.g., Y. Aikawa et al. 1997; K. Furuya & Y. Aikawa 2014; M. Yu et al. 2016, 2017; A. D. Bosman et al. 2018; K. R. Schwarz et al. 2018; M. Ruaud et al. 2022; K. Furuya et al. 2022) and locking up CO into larger dust bodies that settle toward the midplane (e.g., E. A. Bergin et al. 2010, 2016; M. Kama et al. 2016; S. Krijt et al. 2018, 2020; E. Van Clepper et al. 2022; D. Powell et al. 2022).

An alternative approach was suggested by D. E. Anderson et al. (2019) and L. Trapman et al. (2022b), namely to combine observations of CO and N_2H^+. In the presence of CO-rich gas the formation of N_2H^+ is inhibited and its destruction is increased, making N_2H^+ an excellent tracer of CO-poor gas in protoplanetary disks. By simultaneously fitting CO and N_2H^+, the latter provides an observational estimate of how much CO has been removed from the gas by the processes mentioned previously and therefore how much the CO-based gas mass needs to be corrected to obtain the correct total gas mass. L. Trapman et al. (2022b) showed that gas masses measured from the combination of CO isotopologue and N_2H^+ lines are consistent with HD-based gas masses. This approach was also recently used by L. Trapman et al. (2025) to measure gas masses for 20 of the disks in the AGE-PRO ALMA large program (K. Zhang et al. 2025).

The unprecedented spatial and spectral resolution and sensitivity of the Atacama Large Millimeter/submillimeter Array (ALMA) has made it possible to measure protoplanetary disk masses in a new and completely independent way, namely through gas kinematics (for a review see C. Pinte et al. 2023). Briefly, while the motions of gas in protoplanetary disks are dominated by the gravitational potential of stars modulated by the pressure gradient, the disk self-gravity can leave an observable signature in the gas kinematics from which the disk mass can be measured. In contrast to the methods discussed previously, kinematically measured gas masses trace the total disk mass directly and circumvent the main sources of uncertainty that affect the indirect methods, such as CO chemistry and dust grain properties.

This technique was first applied by B. Veronesi et al. (2021) for the disk around Elias 2-27, and similar mass measurements have been carried out for the five disks in the MAPS ALMA large program (G. Lodato et al. 2023; P. Martire et al. 2024; see also S. M. Andrews et al. 2024; B. Veronesi et al. 2024). In an accompanying Letter C. Longarini et al. (2025) used the rotation curves derived by J. Stadler et al. (2025) from observations from the exoALMA large program (R. Teague et al. 2025) to kinematically measure disk masses of a subset of the exoALMA sample. They focused their attention on 10 disks, for which the geometrical orientation in the sky allows robust constraints on disk masses from self-gravity.

Given the importance of gas disk mass for planet formation, it is crucial that indirect, but more widely applicable, line-flux-based gas masses are compared and benchmarked against

Table 1
Stellar and Disk Parameters

Name	R.A.	Decl.	Distance (pc)	SpT	$T_{\rm eff}$ (K)	L_* ($L_\odot$)	M_* ($M_\odot$)	$F_{1.3\rm mm}$ (mJy)	$M_{\rm dust}$[b] ($M_\oplus$)	PA (deg)	i (deg)	$v_{\rm LSR}$ (km s^{-1})	References
DM Tau	04:33:48.73	18:10:09.97	144	M2	3715	0.24	0.45	104.7	79.3	336	39	6.0	1,2
AA Tau	04:34:55.42	24:28:53.03	135	K7	4350	1.10	0.79	67.0	27.8	273	59	6.4	6
LkCa 15	04:39:17.79	22:21:03.39	157	K5	4365	1.00	1.14	151.0	85.9	62	50	6.2	5
HD 34282	05:16:00.48	−09:48:35.39	309	A0	9520	10.8	1.61	99.0	109.4	117	58	−2.4	11, 13
MWC 758	05:30:27.53	25:19:57.08	156	A7	7850	14.0	1.40	70.7	19.1	240	19	6.0	13, 14
CQ Tau	05:35:58.47	24:44:54.09	149	F2	6890	10.0	1.4	144.0	44.4	235	52	6.1	12, 13
PDS 66	13:22:07.54	−69:38:12.22	98	K1V	5035	1.20	1.28	148.0	30.4	189	32	4.0	7, 8
HD 135344B	15:15:48.45	−37:09:16.02	135	F5	6440	6.70	1.61	117.0	28.1	243	16	7.0	11
HD 143006	15:58:36.91	−22:57:15.22	167	G7	5620	3.80	1.56	59.0	24.6	169	17	7.8	9, 10
RXJ 1615.3-3255	16:15:20.23	−32:55:05.10	156	K5	4350	0.60	1.14	480.0	312.3	325	47	8.0	1
V4046 Sgr	18:14:10.48	−32:47:34.52	72	K5/K7	4370	0.5/0.3[a]	1.73	327.0	47.6	256	34	3.0	3
RXJ 1842.9-3532	18:42:57.98	−35:32:42.83	151	K2	4780	0.80	1.07	63.2	36.6	206	39	6.0	4
RXJ 1852.3-3700	18:52:17.30	−37:00:11.95	147	K2	4780	0.60	1.03	58.2	33.2	147	33	5.6	4
GM Aur	04:55:10.98	21:59:54.00	159	K6	4350	1.20	1.10	162.0	88.3	57	53	5.6	15, 16
AS 209	16:49:15.30	−14:22:08.64	121	K5	4266	1.41	1.20	288.0	86.5	86	35	4.6	17, 18
IM Lup	15:56:09.21	−37:56:06.13	158	K5	4266	2.57	1.10	253.0	108.3	144	48	4.5	19, 20
MWC 480	04:58:46.30	29:50:37.00	162	A5	8250	21.9	2.10	253.0	61.9	148	37	5.1	21
HD 163296	17:56:21.30	−21:57:22.00	101	A1	9355	17.0	2.00	715.0	73.0	133	47	4.8	11
Elias 2-27	16:26:45.0	−24:23:7.8	116	M0	3850	0.92	0.49	330.0	103.9	119	56	2.0	18

Notes.
[a] V4046 Sgr is a compact binary system. The table lists the spectral type (SpT) and stellar luminosity for both its stars.
[b] Dust masses are computed from the 1.3 mm continuum flux using $M_{\rm dust} = F_{1.3\rm mm} d^2/\kappa_\nu B_\nu(T)$ assuming $\kappa_\nu = 2.3 \times (\nu/230\,\rm GHz)\,cm^2\,g^{-1}$ and $T = 20$ K (see S. V. W. Beckwith et al. 1990; C. F. Manara et al. 2023). References: M_*, i, and position angle (PA) from A. F. Izquierdo et al. (2025), R.A., decl., and distance from Table 1 of R. Teague et al. (2025).
References. 1: G. H. Herbig (1977), 2: S. M. Andrews et al. (2011), 3: J. Bouvier et al. (1999), 4: S. M. Andrews et al. (2018a), 5: J. R. Fairlamb et al. (2015), 6: J. Guzmán-Díaz et al. (2021), 7: B. Acke et al. (2005), 8: G. H. Herbig (1960), 9: E. E. Mamajek et al. (2002), 10: Á. Ribas et al. (2023), 11: K. L. Luhman & E. E. Mamajek (2012), 12: S. A. Barenfeld et al. (2016), 13: G. R. Quast et al. (2000), 14: C. F. Manara et al. (2014), 15: C. Espaillat et al. (2010), 16: E. Macías et al. (2018), 17: G. H. Herbig & K. R. Bell (1988), 18: S. M. Andrews et al. (2009), 19: J. M. Alcalá et al. (2017), 20: J. M. Alcalá et al. (2019), 21: B. Montesinos et al. (2009).

kinematically measured gas masses. In this work we carry out this benchmark and present new N_2H^+ $J = 3$–2 ALMA Band 7 observations of 11 disks and new $C^{18}O$ $J = 2$–1 observations for one disk (RXJ 1842.9-3532). We combine these observations with archival ALMA observations of N_2H^+, ^{13}CO, and $C^{18}O$ to measure gas disk masses for 19 disks, which we compare to kinematically based gas masses from the literature (B. Veronesi et al. 2021; P. Martire et al. 2024; C. Longarini et al. 2025).

The structure of this Letter is as follows. In Section 2 we outline our sample and describe the calibration and imaging of the new and archival observations. In Section 3 we describe how we measure gas mass from these observations. Section 4 analyzes these gas masses and compares them to the kinematically measured gas masses. These results are discussed in Section 5 and we present our conclusions in Section 6.

2. Observations and Sample

2.1. Sample

The sample discussed in this work differs somewhat from the exoALMA disk sample (R. Teague et al. 2025). Of the 15 exoALMA disks, all but two, SY Cha and RXJ 1604-3010 A, have observations of N_2H^+ (3–2) and ^{13}CO and $C^{18}O$ (2–1) or (3–2) available in the ALMA archive or presented in this work. As we will discuss in Section 3 these lines are needed to measure the gas mass, so we limit our analysis to these 13 disks. For nine of the 13 disks C. Longarini et al. (2025) were able to measure kinematic gas masses from the rotation curves presented by J. Stadler et al. (2025). The remaining four disks were either too face-on or their emission was too asymmetric to obtain reliable kinematic gas masses (see C. Longarini et al. 2025 for details). While this prevents us from performing a gas mass comparison with kinematics, we do include these four disks in our other analyses.

We supplement our 13 exoALMA disks with six disks where kinematically measured gas masses are also available (B. Veronesi et al. 2021; P. Martire et al. 2024) to maximize the number of disks with such measurements in our sample. These are the five disks from the MAPS large program (K. I. Oberg et al. 2021) and Elias 2-27 (e.g., L. M. Pérez et al. 2016; T. Paneque-Carreño et al. 2021). These six disks also have the necessary line fluxes available to measure their gas masses. Our full sample thus consists of 19 disks, 15 of which have kinematically measured gas masses. Stellar and disk parameters of the sample are summarized in Table 1.

2.2. New Observations

We present new ALMA Band 7 observations of N_2H^+ $J = 3$–2 for AA Tau, CQ Tau, MWC 758, RXJ 1615.3-3255, RXJ 1852.3-3700, RXJ 1842.9-3532, PDS 66, HD 34282, HD 143006, HD 135344B, and Elias 2-27 (IDs 2022.1.00485.S, 2023.1.00334.S; PI: L. Trapman). We also present ALMA Band 6 observations of $C^{18}O$ (2–1) and $C^{17}O$ 2–1 for RXJ 1842.9-3532 (ID 2023.1.00334.S).

The ALMA Band 6 and 7 observations were carried out from 2023 October to 2024 May for program 2023.1.00334.S, with baseline lengths between 15 and 1200 m and from 2022 October to 2023 January for program 2022.1.00485.S, with baseline lengths between 15 and 740 m.

The Band 7 correlator was set up to cover N_2H^+ (3–2) at 279.517 GHz, DCO^+ 4–3 at 288.149 GHz, DCN 4–3 at 289.65 GHz, $C^{34}S$ 6–5 at 189.215 GHz, and H_2CO $4_{0,4}$–$3_{0,3}$ at 290.623 GHz. All lines are covered at a spectral resolution of 122 kHz ($\sim$120 m s^{-1}) with the exception of H_2CO, which was covered at a coarser spectral resolution of 977 kHz (1.2 km s^{-1}). In addition to the lines the correlator setup also includes two 1.875 GHz wide continuum spectral windows centered at 278.008 GHz and 290.870 GHz, respectively. Note that the window at the higher frequency is the same spectral window that covers the H_2CO line, which is why it has a coarser spectral resolution.

The Band 6 correlator was set up to cover the $C^{18}O$ (2–1) line at 219.565 GHz, $C^{17}O$ 2–1 at 224.719 GHz, SO_2 $4_{2,2}$–$3_{1,3}$ at 235.156 GHz, $HCC^{13}CN$ 26–25 at 235.514 GHz, $HC^{13}CCN$ 26–25 at 235.537 GHz, and HCCCN 26–25 at 236.517 GHz. All lines are covered at a spectral resolution of 122 kHz ($\sim$150 m s^{-1}) with the exception of $C^{18}O$ (2–1), which is covered at a higher spectral resolution of 61 kHz (83.3 m s^{-1}). In addition to the lines the correlator setup also includes a 1.875 GHz wide continuum spectral window centered at 237.063 GHz.

The on-source times for Band 7 and Band 6 were 30–50 minutes and 40 minutes, respectively. The observational details are summarized in Table A1.

2.2.1. Data Reduction

All observations were initially calibrated using the Common Astronomy Software Application (CASA; CASA-Team et al. 2022) pipeline version 6.4.1.12 for program 2022.1.00485.S and 6.5.4.9 for program 2023.1.00334.S using the `scriptforPI.py` as provided with the data.

The signal-to-noise ratio (SNR) of our observations was high enough to conduct self-calibration after the initial pipeline calibration. Our approach was based on the self-cal procedures of the DSHARP, MAPS, and AGE-PRO large programs (e.g., S. M. Andrews et al. 2018b; I. Czekala et al. 2021; K. Zhang et al. 2025). It is nearly identical to the exoALMA self-calibration procedure, with the exception of the spatial alignment (see R. Loomis et al. 2025 for details).

First, continuum-only visibility data sets were created by flagging all channels within $\pm$20 km s^{-1} of one of the lines in our spectral setup, irrespective of whether this line was detected or not. The resulting line-free continuum channels were averaged together into channels with a maximum width of 125 MHz. Next, individual execution blocks were astrometrically aligned by fitting 2D Gaussians to their continuum emission in the image plane and aligning their phase centers to the coordinates listed in Table 1. For HD 135344B, HD 143006, HD 34282, and MWC 758 the continuum emission was found to be too asymmetric to be reliably fitted with a Gaussian. Here we instead fitted the data with a Gaussian ring, using its center to align the measurement sets.

After alignment we checked relative flux scaling between execution blocks by deprojecting the continuum visibilities using disk geometry from the literature (see Table 1) and comparing their amplitude profile as a function of baseline length. In all cases we found the fluxes of individual execution blocks for a single source to differ by less than 10%. As this is within the expected absolute flux uncertainty of ALMA we did not rescale the fluxes.

Self-calibration was then carried out first on just the short-baseline observations, followed by a second self-calibration using the combined self-calibrated short-baseline and non-self-calibrated long-baseline observations. For both self-calibration sets we performed 1–3 rounds of phase-only self-calibration followed by a single round of amplitude+phase self-calibration. For the phase-only rounds the initial solution interval was chosen to be the full on-source time. Each consecutive round reduced that interval by a factor of 2, ending when the current phase-only solution improved the peak SNR by less than 10% compared to the previous solution.

After self-calibration the obtained gain tables were applied to the full visibility data set, followed by a subtraction of the continuum using the task `uvcontsub`. For each spectral window we flag all channels within $\pm$20 km s^{-1} of each line in the spectral setup before fitting the remaining channels with a first-order polynomial.

2.2.2. Imaging

The lines and continuum were imaged with the CASA task `tclean` using the "multiscale" deconvolver with scales of [0, 5, 15] 0.″02 pixels, a "Briggs" weighting with a robust parameter of 0.5, a gain of 0.08, and a small scale bias of 0.45. The images were cleaned down to a threshold of 1σ, measured from an emission-free part of the cube. For imaging the lines we also include a Keplerian mask created using the routine from R. Teague (2020) with the parameters listed in Table 1. This results in a typical beam of $\sim$0.″25 − 0.″35 and sensitivities of $\sim$3–5 mJy beam^{-1} per 0.25 km s^{-1} channel.

2.3. Archival Observations

In addition to the new N_2H^+ (3–2) observations presented in this work we also make use of a large set of archival observations, primarily ones that provide ^{13}CO and $C^{18}O$ observations for our sources. In most cases these are of the $J = 2$–1 transition, but for RXJ 1615.3-3255, AA Tau, HD 143006, and HD 135344B, observations of this transition were not available in the ALMA archive so the $J = 3$–2 transition is used instead. For Elias 2-27 observations of $J = 2$–1 are available but show significantly more cloud contamination than the $J = 3$–2 observations. We therefore opt to use the latter transition here. Table A2 in the Appendix summarizes the program IDs of the archival data sets, and for further details on the observations and data reduction of each we refer the reader to the works listed in the table.

For two sources, RXJ 1615.3-3255 and HD 143006, one or both of the CO isotopologue archival observations have not previously appeared in the literature. For these sources we

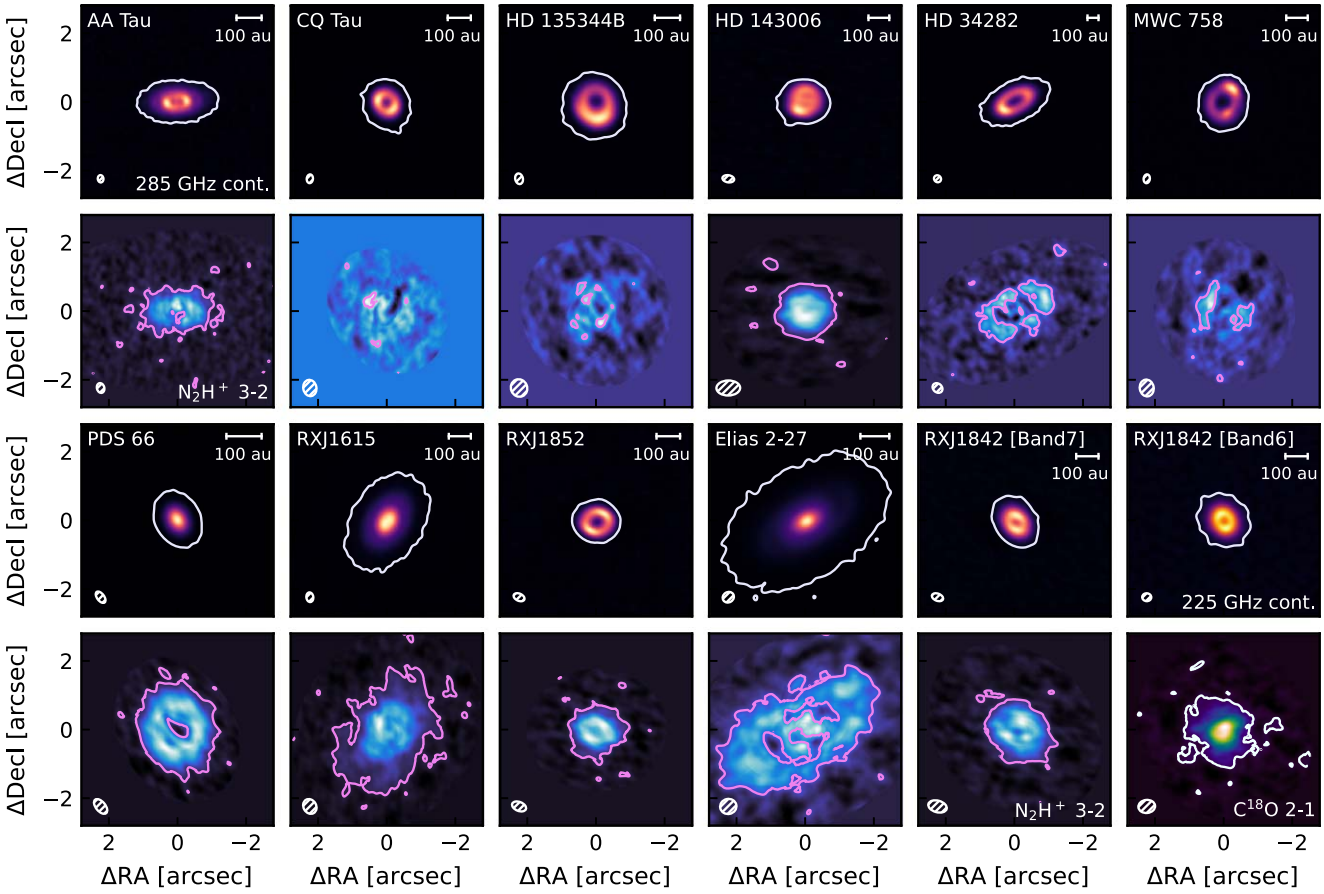

Figure 1. Gallery of the new ALMA Band 6 and 7 observations presented in this work. Colors are peak-normalized for each individual panel. For each source the 285 GHz continuum is shown first, with its N_2H^+ (3–2) integrated intensity map shown directly below that. Note that the last two panels show the Band 6 225 GHz and $C^{18}O$ (2–1) observations of RXJ 1842.9-3532. White (except for $C^{18}O$) and pink contours denote 5σ and 3σ, respectively. The white contours for $C^{18}O$ also show 3σ.

calibrated, self-calibrated, and imaged the archival data following the same procedure as was used for the new observations. A more in-depth analysis of the CO isotopologue observations of HD 143006 will be presented by S. E. van Terwisga et al. (2025, in preparation).

2.4. A First Look at the Observations

Integrated intensity maps of the 285 GHz continuum and N_2H^+ of each source in our sample are presented in Figure 1. While some of the disks exhibit substructures, this work will focus on the gas mass derived from integrated fluxes, and the analysis of the resolved emission will be presented in a future work.

To measure integrated fluxes, the data cubes were first corrected for the non-Gaussian beam resulting from multi-configuration ALMA observations following I. Czekala et al. (2021) (so-called JvM correction, see also S. Jorsater & G. A. van Moorsel 1995). In the case of line emission, integrated intensity maps were created using the same Keplerian mask used for imaging. From the resulting 2D images the integrated flux was measured using a curve-of-growth method.[33] Here the flux is measured using increasingly larger elliptical apertures with the same aspect ratio and orientation as the disk until te integrated flux plateaus. We note that this method was only used to measure fluxes from the new observations and the archival observations where integrated fluxes had not been previously published. For sources where CO isotopologue or N_2H^+ integrated line fluxes were already available we adopt the published values to maintain consistency with existing literature. The integrated line and continuum fluxes are summarized in Table A2.

Figure 2 shows the integrated line and continuum fluxes from this work combined with the 20 class II disks from the AGE-PRO ALMA large program first presented by D. Deng et al. (2025) and C. Agurto-Gangas et al. (2025). Note that for $C^{18}O$ we have scaled down the $C^{18}O$ (3–2) line fluxes by a factor of 2.3, which is the median $C^{18}O$ (3–2)/$C^{18}O$ (2–1) flux line ratio for thermochemical models with $M_{\rm disk} \geqslant 10^{-4}\,M_\odot$ from L. Trapman et al. (2025). Starting from the top panel of Figure 2, we see a correlation between $C^{18}O$ and 225 GHz continuum fluxes, which is in line with earlier works (e.g., J. B. Bergner et al. 2019; D. E. Anderson et al. 2024; D. Deng et al. 2025; C. Agurto-Gangas et al. 2025). The combined sample of the three ALMA large programs—MAPS, AGE-PRO, and exoALMA—shows that this correlation holds over more than three orders of magnitude in both continuum and $C^{18}O$ flux.

If the Herbig disks are excluded, a similar positive correlation can be seen between N_2H^+ (3–2) and the 285 GHz continuum fluxes for the T Tauri disks, also in line

[33] As implemented in https://zenodo.org/records/14973489.

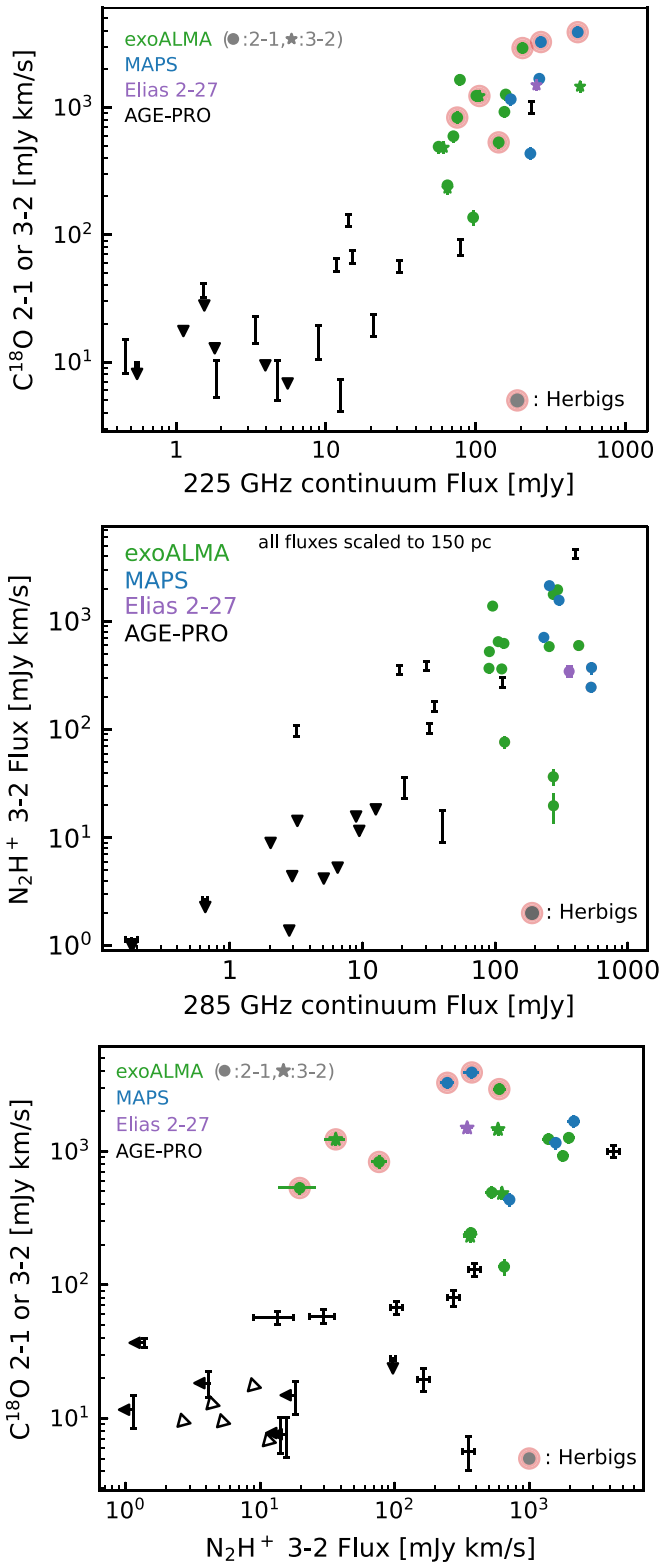

Figure 2. Integrated line and continuum fluxes, scaled to a distance of 150 pc, of the disk sample examined in this work (in green, blue, and purple) combined with 20 class II disks from the AGE-PRO ALMA large program, shown in black (D. Deng et al. 2025; C. Agurto-Gangas et al. 2025). $C^{18}O$ (2–1) and (3–2) observations are denoted as circles and stars, respectively. The $C^{18}O$ (3–2) fluxes are reduced by a factor of 2.3, the median $C^{18}O$ (3–2)/$C^{18}O$ (2–1) line ratio of models with $M_{\rm disk} \geqslant 10^{-4}\,M_{\odot}$ from L. Trapman et al. (2025). Herbig disks are highlighted with a pink circle. Triangles show upper limits, with open triangles representing upper limits in both N_2H^+ and $C^{18}O$.

with previous findings (e.g., D. E. Anderson et al. 2022, 2024; D. Deng et al. 2025; C. Agurto-Gangas et al. 2025). It is unclear whether the same correlation is also present for faint ($\lesssim$10 mJy) continuum sources due to the low detection rate of N_2H^+ (3–2) below that point. It should also be noted that, while suggestive, the trend of N_2H^+ upper limits with continuum flux is an artifact of the correlation between continuum flux and continuum disk size (e.g., A. Tripathi et al. 2017; N. Hendler et al. 2020). For the N_2H^+ nondetections the size of the continuum dust disk was used as the aperture size for many sources, which when combined with the continuum flux–size relation leads to a positive correlation between the N_2H^+ upper limit threshold and the continuum flux (see D. Deng et al. 2025; C. Agurto-Gangas et al. 2025 for details).

The middle panel of Figure 2 also shows that the Herbig disks in the sample do not follow the same N_2H^+–continuum flux correlation as is seen for the T Tauri disks. For Herbig disks of a given continuum flux the N_2H^+ (3–2) integrated flux is approximately an order of magnitude fainter. A likely cause of this is the higher stellar luminosities of these sources warming up the disk. This results in less CO freeze-out and therefore a higher CO abundance that inhibits the formation of N_2H^+ (e.g., C. Qi et al. 2015). Curiously, the N_2H^+ flux of Elias 2-27, itself an M0 T Tauri star, lies closer to the Herbig disks than to the T Tauri disks. A possible explanation could be the young age of the system, with active accretion through the disk and backwarming by an envelope increasing the disk temperature to levels similar to those in the Herbig disks (e.g., P. D'Alessio et al. 1998; B. A. Whitney et al. 2013; M. L. R. van 't Hoff et al. 2018, 2020; A. Kuznetsova et al. 2022). An alternative explanation could be a low midplane ionization rate in this source, which we will discuss further in Section 5.3.

The bottom panel of Figure 2 shows $C^{18}O$ set against N_2H^+. Again excluding the Herbig disks, we see that above a $C^{18}O$ flux of $\sim$100 mJy km s^{-1} the two lines are correlated, similar to what was recently found by D. E. Anderson et al. (2024). As discussed by these authors this correlation is unexpected given the anticorrelation between CO and N_2H^+, but it could suggest that other factors, such as disk mass and size, dominate over chemical effects. Alternatively, a correlation would also be expected if CO abundances are similar between disks (e.g., D. Deng et al. 2025; C. Agurto-Gangas et al. 2025). It is unclear whether the correlation extends below this threshold. N_2H^+ is only detected for six of the 18 sources with a $C^{18}O$ flux $\leqslant$100 mJy km s^{-1}, but one of those detections is for the source with the faintest $C^{18}O$ detection in the figure. As these are all AGE-PRO sources we refer the reader to D. Deng et al. (2025) and C. Agurto-Gangas et al. (2025) for a more detailed analysis.

As in the middle panel, the Herbig disks and Elias 2-27 occupy a different part of the figure. These sources have N_2H^+ fluxes that are $\sim$1–2 orders of magnitude lower than those of T Tauri disks with similar $C^{18}O$ fluxes. Located in between the Herbigs and the T Tauris is the disk around HD 143006, a star of spectral type G7 whose stellar luminosity lies in between those of the T Tauri and Herbig stars that make up our sample. Its location in the bottom panel of Figure 2 is consistent with the idea that a higher overall disk temperature, driven by a higher stellar luminosity, is what sets apart Herbig and T Tauri disks.

3. Measuring Gas Disk Masses from Line Emission

For measuring the gas disk masses ($M_{\rm gas}$) in our sample we follow the approach of L. Trapman et al. (2025) using the grid of thermochemical models presented in the same work. To briefly summarize this approach: L. Trapman et al. (2025) used the thermochemical code DALI (S. Bruderer et al. 2012; S. Bruderer 2013) to run a large grid of disk models where they varied the disk mass, characteristic size, stellar luminosity, vertical structure, and dust properties. These models include isotope-selective photodissociation and chemistry for CO following A. Miotello et al. (2014), but they do not include the processes thought to be responsible for removing CO from the gas in the CO-emitting layer. Instead, in their models the peak CO abundance in the CO-emitting layer is included as a free parameter ($3\times10^{-7}\leqslant x_{\rm CO}\leqslant10^{-4}$), which serves as a proxy for processes beyond photodissocation and freeze-out that affect gaseous CO in the disk. Constraining this parameter is the main reason for including N_2H^+ in addition to the CO lines, as it breaks the degeneracy between disk mass and $x_{\rm CO}$ encountered when only using CO lines (e.g., D. E. Anderson et al. 2019, 2022; L. Trapman et al. 2022b; K. I. Öberg et al. 2023).

Using synthetic observations from this model grid, they used a Markov Chain Monte Carlo (MCMC) procedure to carry out a χ^2 fit of the observed 225 GHz continuum, ^{13}CO (2–1), C^{18}O (2–1), and N_2H^+ (3–2) integrated line fluxes and derive a posterior distribution for the disks in AGE-PRO (see L. Trapman et al. 2025 for further details).

In this work we make a few small modifications to this approach. First, we use $10^{-4}\,M_\odot\leqslant M_{\rm gas}\leqslant0.5\,M_\odot$ as a prior for the disk mass, which is in line with the fact that the sources in this work are much brighter and likely more massive than the AGE-PRO disks. This prior is assumed to be uniform in log-space as the gas mass is also fit in log-space. Second, six T Tauri sources in our sample have stellar luminosities $L_*\geqslant1\,L_\odot$, which is the maximum stellar luminosity in the L. Trapman et al. (2025) model grid. As fitting the observations with a low stellar luminosity could lead to an overestimation of the amount of CO freeze-out and thus an overestimation of the gas disk mass, we ran an extra series of models[34] with $L_*=3.0$ $L_\odot$, varying all other parameters as in L. Trapman et al. (2025), except that we skip $R_{\rm c}=1$ au and $M_{\rm gas}<10^{-4}\,M_\odot$ as these models would be too compact and/or low-mass to represent the disks in our sample.

It is also worth pointing out that many of the sources in the sample have large dust cavities and/or other dust substructures (e.g., Figure 1; L. M. Pérez et al. 2015; T. Paneque-Carreño et al. 2021; A. Sierra et al. 2021; P. Curone et al. 2025), which are not present in thermochemical models. We will revisit their impact on our results in Section 5.2.

The Herbig disks in our sample, i.e., HD 135344B, HD 34282, CQ Tau, MWC 758, HD 163296, and MWC 480, warrant a slightly different approach. The models of L. Trapman et al. (2025) were run using stellar properties typical for T Tauri stars ($T_{\rm eff}=3500$–4000 K; $L_*=0.1$–1.0 $L_\odot$), making them not representative for these sources. Recently, L. M. Stapper et al. (2024) presented a large grid of thermochemical models for Herbig disks, which they used to measure gas masses for a large sample of Herbig disks. In order to have a method for measuring gas mass that is as consistent as possible for both T Tauri and Herbig disks we use the model grid from L. M. Stapper et al. (2024) and fit the observations—in this case the ^{13}CO and C^{18}O—using a similar MCMC method to that used for the T Tauri disks. For consistency we also compare our derived Herbig gas disk masses with the values obtained by L. M. Stapper et al. (2024), finding excellent agreement between the two estimates of gas mass, with gas masses being within a factor of ~3 (1σ) of each other.

It should be noted here that the models from L. M. Stapper et al. (2024) do not include the peak CO abundances as a free parameter. Several studies find that CO in Herbig disks is underabundant by an order of magnitude (e.g., T. Paneque-Carreño et al. 2025; G. Rosotti et al. 2025). However, as we will show in Section 5.4, including the CO abundance as a free parameter and fitting N_2H^+ in addition to the CO lines does not significantly change the derived gas mass.

[34] The fluxes for these models and the ones presented in Section 5.2 and 5.4 are available at Zenodo DOI: 10.5281/zenodo.15148628.

4. Results

4.1. Line-based Gas Disk Masses

Figure 3 shows the gas masses derived from fitting the 225 GHz dust continuum and ^{13}CO, C^{18}O, and N_2H^+ integrated line fluxes. The gas masses are also summarized in Table 2. We find overall high gas masses in the range of $\sim$0.01–0.1 $M_\odot$, which is unsurprising as the disks in the sample are among the brightest, and therefore most massive and/or largest, protoplanetary disks in the solar neighborhood (e.g., K. I. Oberg et al. 2021; R. Teague et al. 2025).

In Figure 4 we plot $M_{\rm gas}$ against the dust mass, computed from the continuum flux assuming a disk-averaged temperature of 20 K and optically thin emission (see also R. H. Hildebrand 1983; M. Ansdell et al. 2016; C. F. Manara et al. 2023). We find gas-to-dust mass ratios between $\sim$80 and $\sim$530 for the 19 sources examined here, similar to what is found by C. Longarini et al. (2025) using the kinematically measured gas masses and dust masses derived from the 870 μm continuum flux. This is a factor of a few higher than the typical ISM value of $\sim$100, which could indicate significant grain growth and inward radial drift. However, given the continuum brightness of our sources it is also very likely that their continuum emission is optically thick, in which case the gas-to-dust mass ratio here represents an upper limit.

Also shown in Figure 4 are the 20 class II disks from the AGE-PRO ALMA large program (K. Zhang et al. 2025). Their gas masses and gas-to-dust ratios are discussed extensively by L. Trapman et al. (2025). We include them here mostly to highlight that in terms of both dust and gas mass the MAPS, AGE-PRO, and exoALMA large programs sample different groups of objects (see K. I. Oberg et al. 2021; R. Teague et al. 2025; K. Zhang et al. 2025).

4.2. Comparing with Gas Disk Masses from Kinematics

Figure 5 shows a comparison of the line emission-based gas masses from this work and kinematically measured gas masses from B. Veronesi et al. (2021), P. Martire et al. (2024), and C. Longarini et al. (2025) for 15 disks. Note that for five disks —AA Tau, RXJ 1615.3-3255, RXJ 1852.3-3700, PDS 66, and AS 209—the kinematically measured gas mass is an upper limit, set to $M_{\rm disk}/M_*=5\%$ (see P. Martire et al. 2024; C. Longarini et al. 2025 for details on these sources). For the five MAPS disks covered by P. Martire et al. (2024) we have

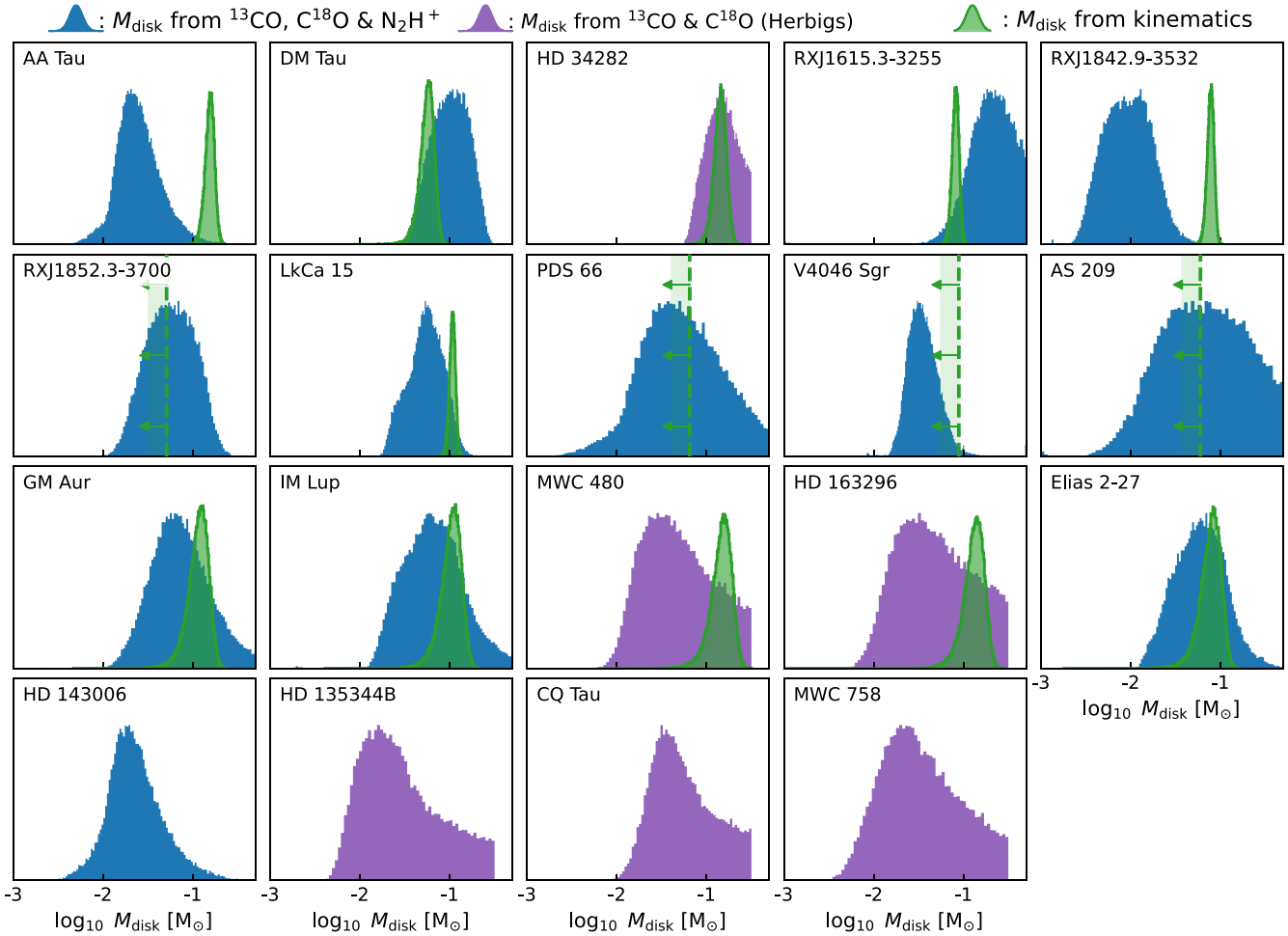

Figure 3. Gas disk mass posteriors obtained from fitting either ^{13}CO, C^{18}O, N_2H^+, and the 225 GHz continuum for the T Tauri disks (shown in blue) or ^{13}CO, C^{18}O, and the 225 GHz continuum for the Herbig disks (shown in purple). In green we show the posteriors of gas disk masses derived from the disk kinematics by B. Veronesi et al. (2021), P. Martire et al. (2024), and C. Longarini et al. (2025). Gas mass upper limits from kinematics, taken to be 5% of the stellar mass (e.g., S. M. Andrews et al. 2024; B. Veronesi et al. 2024), are shown as a green vertical dashed line.

adopted minimum gas mass uncertainties of 25% of the measured gas disk mass as recommended by S. M. Andrews et al. (2024) and B. Veronesi et al. (2024).

Overall the two methods agree with each other within their respective errors. Quantitatively, we find that the two gas mass estimates agree within 1σ–2σ and lie within a factor of 2–3 of each other. Interestingly we also see that the line-based gas disk masses are consistently lower than the kinematically measured gas masses. Assuming that the kinematically measured gas masses represent the true disk mass, this suggests that the line-based gas mass, or at least our method of deriving it, underestimates the true disk mass by a small factor. To quantify this factor we compute the median ratio using a Kaplan–Meier estimator. To incorporate the uncertainties on each gas mass we repeat this process 10,000 times, each time drawing random line emission-based and kinematically measured gas masses from their respective posterior distributions. We find that the dynamical masses in our sample are on average $2.3^{+0.7}_{-1.0}\times$ higher than the CO + N_2H^+ gas masses. We will discuss possible explanations for this in more detail in Section 5.1.

Three sources show large differences between their two gas disk mass estimates. RXJ 1842.9-3532 and AA Tau have CO + N_2H^+ gas masses that are $\sim$5$\times$ lower than their kinematically measured gas masses, while the CO + N_2H^+ gas mass of RXJ 1615.3-3255 is $\gtrsim$4$\times$ larger than its kinematically measured one. For AA Tau the uncertainties on the gas mass from kinematics are large due to its high inclination and difficulties in extracting its thermal structure (see M. Galloway-Sprietsma et al. 2025; C. Longarini et al. 2025). As a result of this its two gas estimates are within 2σ of each other, similar to many of the other sources. For RXJ 1842.9-3532 the uncertainties on both gas measurements are too small to explain their difference. From the kinematics side, a possible explanation could be that in the inner disk the heights of ^{12}CO and ^{13}CO emission overlap, thereby complicating the extraction of the temperature structure. From the chemistry side, a low midplane ionization rate ($\zeta_{mid} \lesssim 10^{-19}$ s^{-1}) and/or an underabundance in N_2 could cause us to underestimate the CO + N_2H^+ gas mass of RXJ 1842.9-3532. The difference for RXJ 1615.3-3255 is harder to explain. As we will discuss in more detail in Section 5.1, possible biases in the CO + N_2H^+ gas mass measurement are more likely to underestimate the true disk mass. And kinematically this source does not show any obvious signs that could indicate that its kinematically measured mass is underestimated. It is worth mentioning that, using CO + N_2H^+, RXJ 1615.3-3255 has a star-to-disk mass ratio of $\sim$0.2, which would have left a detectable kinematic signature (see S. M. Andrews et al. 2024; B. Veronesi et al. 2024).

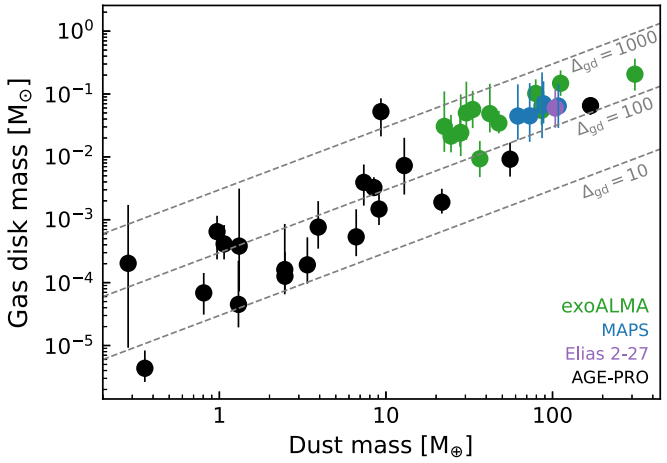

Figure 4. Emission line-based gas disk masses vs. dust masses for the 19 sources examined in this work plus the 20 class II disks from the AGE-PRO ALMA large program (C. Agurto-Gangas et al. 2025; D. Deng et al. 2025; L. Trapman et al. 2025; K. Zhang et al. 2025). Note that the 1.3 mm flux used to derive the dust mass is very likely at least somewhat optically thick for the brightest sources, so dust masses $\gtrsim$20 $M_\oplus$ should be considered lower limits of the true dust mass. Gray dashed lines show gas-to-dust mass ratios of 10, 100, and 1000.

Table 2
Emission Line-based Gas Masses

name	$M_{\rm gas}$ ($M_\odot$)	$\log_{10} x_{\rm CO}$	$\log_{10} \zeta_{\rm mid}$ (s^{-1})
DM Tau	$0.102^{+0.064}_{-0.042}$	$-4.24^{+0.15}_{-0.21}$	$-17.75^{+0.68}_{-0.82}$
V4046 Sgr	$0.035^{+0.018}_{-0.010}$	$-4.60^{+0.20}_{-0.21}$	$-17.62^{+0.91}_{-0.97}$
RXJ 1615.3-3255	$0.207^{+0.148}_{-0.090}$	$-4.12^{+0.08}_{-0.12}$	…
RXJ 1852.3-3700	$0.057^{+0.052}_{-0.027}$	$-4.54^{+0.22}_{-0.24}$	$-16.94^{+0.64}_{-0.98}$
RXJ 1842.9-3532	$0.009^{+0.008}_{-0.004}$	$-4.60^{+0.21}_{-0.22}$	…
LkCa 15	$0.055^{+0.031}_{-0.022}$	$-4.46^{+0.20}_{-0.21}$	$-18.66^{+1.03}_{-0.84}$
AA Tau	$0.024^{+0.020}_{-0.009}$	$-4.60^{+0.24}_{-0.22}$	$-17.71^{+0.98}_{-1.21}$
PDS 66	$0.050^{+0.102}_{-0.031}$	$-5.53^{+0.28}_{-0.29}$	$-17.55^{+0.96}_{-0.94}$
HD 143006	$0.021^{+0.024}_{-0.009}$	$-5.11^{+0.25}_{-0.23}$	…
HD 135344B	$0.024^{+0.071}_{-0.014}$	$-4.13^{+0.10}_{-0.17}$	…
CQ Tau	$0.049^{+0.092}_{-0.024}$	$-4.50^{+0.30}_{-0.08}$[a]	…
HD 34282	$0.148^{+0.082}_{-0.052}$	$-4.11^{+0.07}_{-0.12}$	…
MWC 758	$0.031^{+0.076}_{-0.018}$	$-4.25^{+0.15}_{-0.21}$	…
GM Aur	$0.069^{+0.072}_{-0.029}$	$-4.38^{+0.21}_{-0.23}$	$-18.66^{+0.81}_{-0.77}$
AS 209	$0.087^{+0.132}_{-0.055}$	$-4.68^{+0.25}_{-0.26}$	$-16.80^{+0.54}_{-0.85}$
IM Lup	$0.041^{+0.037}_{-0.018}$	$-4.45^{+0.21}_{-0.20}$	$-18.52^{+0.70}_{-0.79}$
MWC 480	$0.066^{+0.057}_{-0.020}$	$-4.22^{+0.15}_{-0.21}$	…
HD 163296	$0.074^{+0.078}_{-0.030}$	$-4.28^{+0.17}_{-0.21}$	…
Elias 2-27	$0.060^{+0.053}_{-0.030}$	$-4.20^{+0.14}_{-0.19}$	$-19.48^{+0.41}_{-0.33}$

Note. Best-fit gas disk masses are the median of $M_{\rm gas}$ posteriors presented in Figure 3, with the uncertainties being the 16th and 84th quantiles of the distribution. Herbig disk CO abundances are from the models discussed in Section 5.4. Midplane ionization rates are from the fits discussed in Section 5.3.
[a] The $x_{\rm CO}$ fit for CQ Tau is bimodal and this value should be viewed with caution (see Section 5.4 for details).

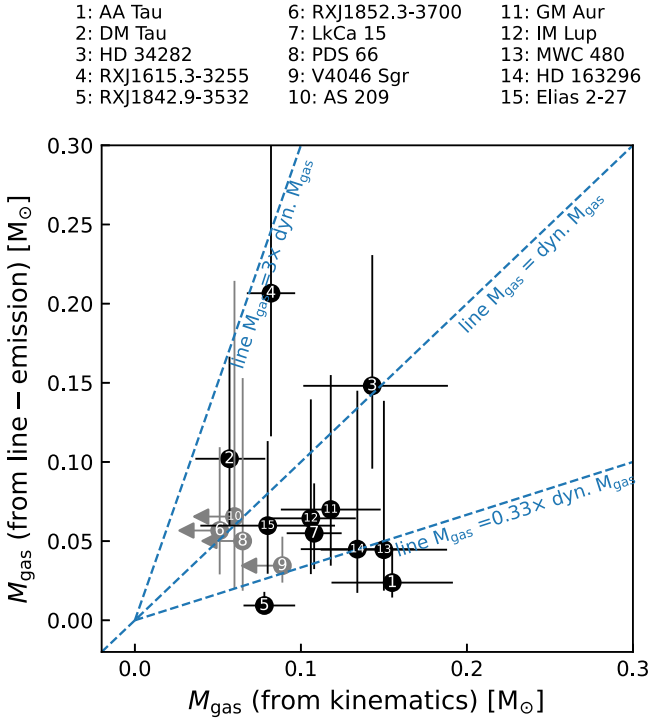

Figure 5. A comparison of the emission line-based and kinematically derived gas disk masses. Kinematic gas mass upper limits are shown in gray. Blue lines show where line-based gas mass is 0.33×, 1×, and 3× the kinematically derived gas mass.

5. Discussion

5.1. Interpreting the (Dis)agreement between the Two Gas Mass Measurement Methods

The previous section showed that emission line-based and kinematically measured gas masses agree with each other, with the former typically being a factor of ∼2× smaller than the latter. This is a promising result given that historically disk mass estimates could differ by up to two orders of magnitude (e.g., A. Miotello et al. 2023). However, we should keep in mind that both methods have their own set of systematic uncertainties. Here we highlight the most important ones for both methods and discuss how this affects the agreement in derived gas masses.

Starting with the kinematically measured gas masses, excellent summaries of the systematics were published by S. M. Andrews et al. (2024) and B. Veronesi et al. (2024). In addition to observational effects such as spatial resolution bias, the main uncertainties for a kinematically measured gas mass are the temperature structure of the disk and the measurement of the emitting surface. The temperature is commonly measured from optically thick CO emission at one or more heights in the disk, depending on the number of available optically thick CO lines (e.g., C. J. Law et al. 2021; M. Galloway-Sprietsma et al. 2025), and must then be extrapolated to the midplane. Tests using both toy models and hydrodynamical simulations suggest that for massive disks ($M_{\rm disk}/M_* \geqslant 0.1$) the true disk mass can be recovered with little bias ($\lesssim$20%) and relatively low uncertainties ($\lesssim$25%) (see S. M. Andrews et al. 2024; B. Veronesi et al. 2024 for details).

Measuring the disk mass from line emission is more indirect than using kinematics because it, by necessity, requires the use of indirect tracers such as CO as proxies for the bulk H_2. Most of the systematic uncertainties therefore arise from the assumptions made in the thermochemical models used to link the emission to the underlying gas mass. L. Trapman et al. (2025) provide a summary of the main uncertainties for the method used in this work to measure line-based gas masses, including the N_2 abundances, midplane ionization rate, and

model assumptions. The first two most likely lead to an underestimation of the gas mass, which could explain why the line-based gas masses are lower than the kinematically measured ones. We will discuss the role of the cosmic-ray ionization rate in more detail in Section 5.3. As for the model assumption, D. Deng et al. (2025) showed that different thermochemical models seem to converge when it comes to the derived gas mass, particularly for the larger, more massive disks.

The vertical temperature structure of the disk can also have an important effect on line fluxes. C. Qi & D. J. Wilner (2024) showed that the presence of a thick vertical isothermal layer causes the CO column density to drop substantially beyond the CO iceline, resulting in a narrow ring of N_2H^+ emission and lower integrated CO isotopologue fluxes (see also C. Qi et al. 2019). The presence of such a layer could therefore explain the difference between the line-based and kinematically measured gas masses. However, C. Qi et al. (2019) also showed that thick vertically isothermal layers are not present in three of their six disk samples, suggesting that they might not be a universal feature of protoplanetary disks.

To summarize, the kinematically measured gas mass provides a more direct measure of the true disk mass. However, it requires the disk to be massive relative to its star ($M_{\rm gas}/M_* \geqslant 0.05$), at intermediate inclination, and overall axisymmetric. Furthermore, measuring the disk mass requires a good understanding of the disk temperature structure and the height of line emission. Conversely, the CO + N_2H^+-based gas mass measurement technique is more broadly applicable as it only requires integrated fluxes and can therefore be applied to a large sample, but it is more indirect and relies on our understanding of CO and N_2H^+ disk chemistry. It is therefore encouraging to see that the two gas mass measurement techniques lie within a small factor (∼2–3×) of each other.

5.2. The Effect of an Inner Dust Cavity on Measuring Gas Masses

As can be seen in Figure 1, a large number of the disks in this sample have large inner dust cavities (see also P. Curone et al. 2025). These cavities are not included in the full disk thermochemical models of L. Trapman et al. (2025), but their presence will have an effect on the temperature structure of the disk (e.g., S. Bruderer 2013; M. Leemker et al. 2022), which could affect the gas mass measurement. To quantify the effect of a dust cavity on our gas masses we ran an additional set of models following the same setup as L. Trapman et al. (2025), but with inner dust cavities of 10, 30, and 60 au. These cavities are included as done, e.g., by S. Bruderer et al. (2012) N. van der Marel et al. (2016), with the dust density inside the cavity set to zero. We do also include a small inner dust disk with a radius of 3 au and a dust depletion factor of 10^{-2}, in line with the typical inner dust disks found in the survey of L. Francis & N. van der Marel (2020). As it is computationally impracticable to rerun the full model grid we only run the dust cavity models for $M_{\rm disk} \in [10^{-4}, 10^{-3}, 10^{-2}, 10^{-1}]\,M_\odot$, $L_* = [0.25, 0.5, 1.0]L_\odot$, and $R_{\rm c} \in [30, 60, 120, 180]$au. As the maximum stellar luminosity of these models is not representative of the Herbigs in our sample we will limit our analysis to the T Tauri disks with dust cavities.

Using these dust cavity models we rederive $M_{\rm gas}$ for six T Tauri disks with observed dust cavities: AA Tau, DM Tau, LkCa 15, RXJ 1842.9-3532, RXJ 1852.3-3700, and V4046 Sgr. These $M_{\rm gas}$ values are measured in the same fashion as is outlined in Section 3 except that the size of the dust cavity is now included as a free parameter, for which we assume a Gaussian prior with a mean equal to the size of the dust cavity from L. Francis & N. van der Marel (2020) and a standard deviation of 10 au (∼0.5× the typical beam of the observations used to measure the size of the dust cavity). Figure 6 shows the resulting gas mass posterior distributions and compares them to the ones obtained using the full disk models. In all cases the gas mass decreases when a dust cavity is included. This is unsurprising as the presence of the cavity increases the overall disk temperature and therefore the line brightness of the CO lines, meaning that the observations can be reproduced with a lower gas mass. However, Figure 6 also shows that this effect is typically small: for the six disks examined there the reduction in gas mass is within a factor of ∼2.5.

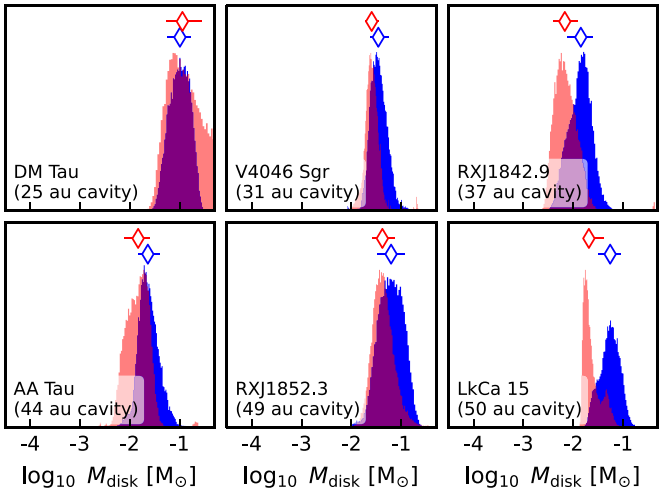

Figure 6. Comparison of the gas mass posteriors obtained using models with (in red) and without (in blue) inner dust cavities. Diamonds and lines above the distribution shows its median value and 16th and 84th quantiles.

5.3. Constraining Midplane Ionization Rates

As an ion, the abundance of N_2H^+ depends on the midplane ionization rate, which is relatively poorly understood in protoplanetary disks (e.g., L. I. Cleeves et al. 2015; R. A. Seifert et al. 2021; Y. Aikawa et al. 2021; D. E. Long et al. 2024). It is therefore one of the main sources of uncertainty for a disk mass obtained from CO isotopologues and N_2H^+. However, given our additional constraints on the gas mass from kinematics, we can also exploit this dependence and use N_2H^+ to constrain the midplane ionization rate. We note here that ionization in the midplane of our models is set with a single ionization rate. In the disk midplane cosmic rays are thought to be the dominant source of ionization, but other sources, e.g., decay of radionuclides, scattered X-rays, can also contribute or even dominate if, e.g., the midplane is shielded (e.g., L. I. Cleeves et al. 2015). The midplane ionization rate discussed here should therefore be interpreted as the sum of these processes. It should also be noted that we are keeping the N_2 abundance fixed, effectively assuming that it is the main nitrogen carrier in the disk. If this is not the case and the N_2 abundance is lower, then the midplane ionization rates derived here would have to be higher to reproduce the observed amount of N_2H^+.

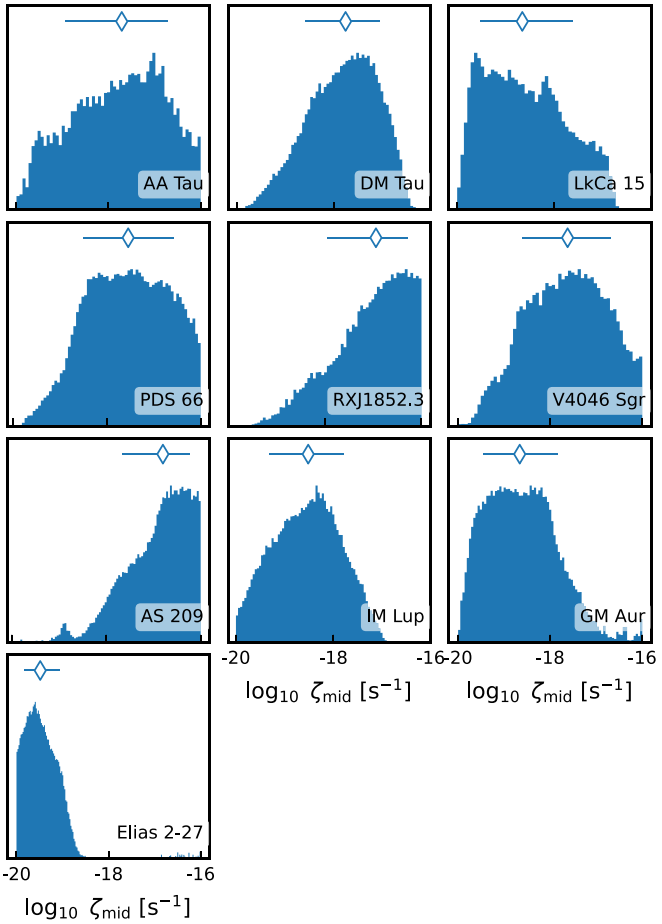

Figure 7. Posterior distributions of the cosmic-ray ionization rate ($\zeta_{\rm mid}$), obtained by refitting the observation using the kinematically measured gas mass and its uncertainties as a prior. Diamonds and lines above the distribution shows its median value and 16$^{\rm th}$ and 84$^{\rm th}$ quantiles.

Figure 7 shows the posterior distributions of $\zeta_{\rm mid}$ where we have refit the observations but now use the kinematically derived gas masses and their uncertainties as a prior during the fit. We exclude RXJ 1842.9-3532 and RXJ 1615.3-3255 as their line-based and kinematic gas masses proved too different from each other to use the kinematic gas mass as a prior while fitting the line emission. Overall we find a wide range of midplane ionization rates, from $\zeta_{\rm mid} \approx 10^{-17}\,{\rm s}^{-1}$ for AS 209 and RXJ 1852.3-3700 to $\zeta_{\rm mid} \approx 3 \times 10^{-20}\,{\rm s}^{-1}$ for Elias 2-27. We find a median ionization rate of $\zeta_{\rm mid} = 1.5 \times 10^{-18}\,{\rm s}^{-1}$. However, the uncertainty of $\zeta_{\rm mid}$ for individual sources is large, typically $\sim$1.5 dex, suggesting that N_2H^+ alone only provides a moderate constraint on the ionization rate.

Comparing our rough, disk-averaged rates to previous studies that used more complex models and observations of multiple ions (e.g., Y. Aikawa et al. 2021; R. A. Seifert et al. 2021; D. E. Long et al. 2024), we find overall agreement. For example, D. E. Long et al. (2024) find a moderate ionization rate of $10^{-18}\,{\rm s}^{-1}$ for DM Tau, which agrees very well with our median value for the source ($\zeta_{\rm mid} = 1.5 \times 10^{-18}\,{\rm s}^{-1}$). Similarly, Y. Aikawa et al. (2021) report midplane ionization rates of $\zeta_{\rm mid} \gtrsim 10^{-18}\,{\rm s}^{-1}$ for AS 209 and IM Lup, and $\zeta_{\rm mid} \lesssim 10^{-18}\,{\rm s}^{-1}$ for GM Aur. For AS 209 and GM Aur our results are in agreement with Y. Aikawa et al. (2021), but for IM Lup we find a somewhat lower value of $\sim 3 \times 10^{-19}\,{\rm s}^{-1}$. However, R. A. Seifert et al. (2021) showed that IM Lup has radially varying midplane ionization rate, with $\zeta_{\rm mid} \lesssim 10^{-20}\,{\rm s}^{-1}$ inside 100 au and $\zeta_{\rm mid} \gtrsim 10^{-17}\,{\rm s}^{-1}$ between 100 and 300 au. As our sole constraint comes from the integrated N_2H^+ flux, we are probing a mix of these two regions, which could explain our overall lower midplane ionization rate.

5.4. The Role of N_2H^+ in Constraining Herbig Gas Disk Masses

In this work we have measured gas masses for T Tauri and Herbig disks in slightly different ways, the largest difference being that for the Herbig disks we do not fit the N_2H^+ observations. Initial gas measurements using CO found that the gas-to-dust mass ratios of T Tauri disks were much lower than the ISM value of $\sim$100 (e.g., J. P. Williams & W. M. J. Best 2014; A. Miotello et al. 2017; F. Long et al. 2017). Comparisons with other gas mass traces such as HD (E. A. Bergin et al. 2013; M. K. McClure et al. 2016) suggested that the CO is underabundant in the warm molecular layer of protoplanetary disks, leading to the inclusion of N_2H^+ as an additional constraint on the gas-phase CO abundance (D. E. Anderson et al. 2019, 2022; L. Trapman et al. 2022b, 2025). For Herbig disks CO-based gas-to-dust mass ratios are routinely found to be at or above the ISM value of $\sim$100 (e.g., L. M. Stapper et al. 2024). This suggests that the processes that reduce the gas-phase CO abundance in T Tauri disks do not significantly affect disks around Herbig stars.

However, this does not exclude the possibility that the gas-phase CO in Herbig disks could be at least mildly underabundant and that their CO-based gas masses could therefore underestimate their true gas masses. Indeed, several studies have found that at least some Herbig disks seem underabundant in CO to some degree (e.g., K. Zhang et al. 2021; T. Paneque-Carreño et al. 2025; G. Rosotti et al. 2025). We can test this hypothesis by fitting the N_2H^+ flux in addition to the CO fluxes, identical to how we fitted the T Tauri disks (see Section 3). Unfortunately the models in L. M. Stapper et al. (2024) do not include synthetic observations of N_2H^+. We therefore ran another set of models analogous to the new $L_* = 3\ L_\odot$ models described in Section 3 but using the observed stellar spectrum of HD 163296 ($L_* = 17\ L_\odot$; O. Dionatos et al. 2019).

Using these models we fit the observations of the six Herbig disks in our sample twice, once where we fit the 1.3 mm continuum and ^{13}CO, C^{18}O, and N_2H^+ line fluxes while having the peak CO abundance be a free parameter and once where we fit the 1.3 mm continuum and ^{13}CO and C^{18}O line fluxes and keep the peak CO abundance fixed (analogous to fitting the Herbig disks using the L. M. Stapper et al. (2024) models). We note the L. M. Stapper et al. (2024) models cover a wider range of parameters relevant for Herbig disks (e.g., L_*, scale height) and have a higher mass resolution than our models. The disk masses derived here therefore do not supersede the ones presented in Section 4.1.

Figure 8 shows the resulting gas mass posteriors for the two fits. For all six source we find that the gas masses are nearly identical, with the mean estimates lying within $\sim$15% of each other. The dual peak structure of the posterior of CQ Tau is due to a lack of models. Its best-fit characteristic radius using the L. M. Stapper et al. (2024) models is $R_{\rm c} \approx 12$ au, while the smallest model in our grid with $M_{\rm disk} = 0.5\,M_\odot$ has $R_{\rm c} = 15$ au. This causes the MCMC procedure to oscillate between these models and models with $M_{\rm disk} = 0.1\,M_\odot$ and $R_{\rm c} = 5$ au, which

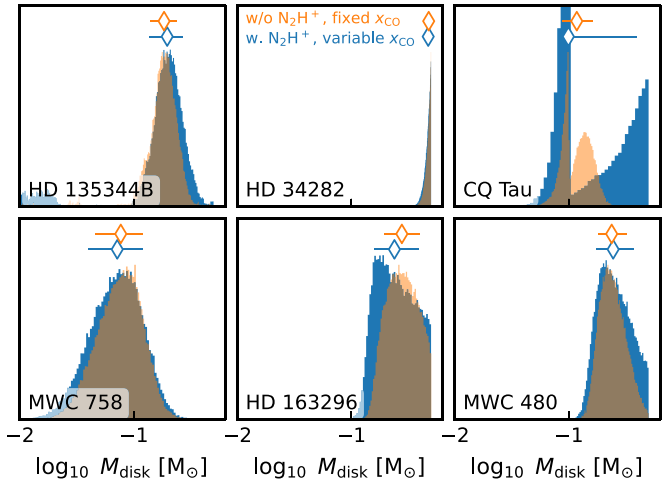

Figure 8. Comparison of the gas mass posteriors for the six Herbig disks for cases where N_2H^+ is excluded from the fit and x_{CO} kept fixed (in orange) and where N_2H^+ is included in the fit and x_{CO} is a free parameter (in blue). Diamonds and lines above the distribution shows its median value and 16th and 84th quantiles.

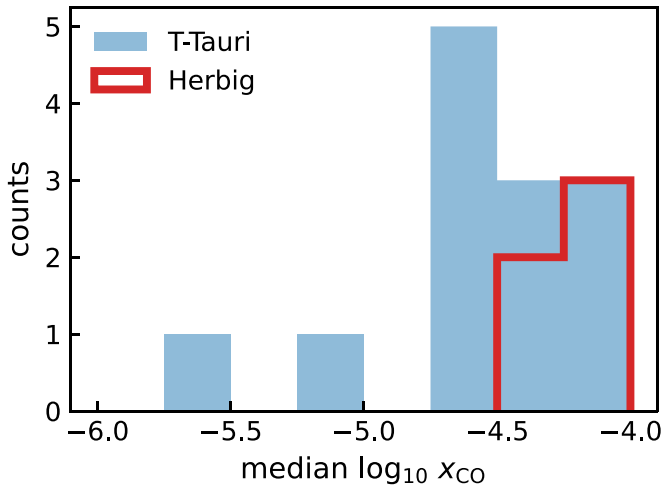

Figure 9. Histogram of the median peak CO abundances, split between the Herbig disks (in red) and the T Tauri disks (in blue).

are included in the grid. Due to this incomplete fit we caution against using x_{CO} for CQ Tau and we have excluded it from our analysis here.

Figure 9 shows a histogram of the median peak CO abundances of the Herbig disks discussed here and the T Tauri disks examined previously. For the Herbig disks we find median values of $\log_{10} x_{CO} \approx -4.35 - 4.1$, which is very close to the ISM value of $\log_{10} x_{CO} \approx -4$. Peak CO abundances of the T Tauri disks are typically lower, peaking at $\log_{10} x_{CO} \approx -4.6$, and they can be as low as $\log_{10} x_{CO} = -5.6$ (Table 2).

This suggests different chemical paths for the T Tauri and Herbig disks, where in the colder T Tauri disks a significant fraction of the gaseous CO freezes out and is converted into less volatile species such as CO_2, whereas in the warmer Herbig disks most of the CO stays in the gas and is not chemically converted (see K. I. Öberg et al. 2023 for a recent review).

The high peak CO abundances found here seem at odds with the lower values found in other works (e.g., K. Zhang et al. 2021; T. Paneque-Carreño et al. 2025; G. Rosotti et al. 2025). T. Paneque-Carreño et al. (2025) and G. Rosotti et al. (2025) independently showed that the height of emission of optically thick CO lines is strongly correlated to both the disk mass and the CO abundance. They found that in order to reproduce the height of CO emission of a number of Herbig disks using the gas mass from previous estimates they need reduce the CO abundance by a factor of up to 10.

One possible explanation of the dichotomy between these works and the results here is that the two methods trace different parts of the disk. The N_2H^+ (3–2) emission predominantly traces the layer between the CO and N_2 icelines (e.g., C. Qi et al. 2013, 2019; M. L. R. van 't Hoff et al. 2017) and is therefore most sensitive to the CO abundance of the gas close to the CO iceline. Conversely, the height of CO emission is most sensitive to the CO abundance at the top of the CO-emitting layer, close to where CO is photodissociated.

We should note here that these results apply specifically for Herbig disks. Similar tests for T Tauri disks show that their gas masses can be ∼3–30× higher and their CO peak gas abundances ∼3−30× lower if N_2H^+ is included with CO when measuring gas masses (e.g., Table 2; see also D. E. Anderson et al. 2019, 2022; L. Trapman et al. 2022a; J. A. Sturm et al. 2023).

6. Conclusions

In this work we have presented new ALMA Band 7 observations of N_2H^+ (3–2) for 11 protoplanetary disks and Band 6 $C^{18}O$ (2–1) observations for one disk. These we combine with archival N_2H^+, ^{13}CO, and $C^{18}O$ observations to measure gas disk masses for 19 disks, primarily from the exoALMA and MAPS ALMA large programs. For the 15 disks where kinematically measured gas masses are available we compare the two gas mass measuring techniques. Our main conclusions are listed below.

1. For T Tauri disks we find clear correlations between the continuum flux and the $C^{18}O$ and N_2H^+ line fluxes similar to what was previously found in the literature. Disks around Herbig stars lie on the same $C^{18}O$–continuum flux correlation, but have 1–2 orders of magnitude lower N_2H^+ fluxes compared to T Tauri disks with similar continuum fluxes. This is likely due to the higher overall temperature and lower CO freeze-out in these disks, resulting in less CO-poor gas and therefore lower overall N_2H^+ abundances.
2. We find overall high gas masses between ∼0.01 and 0.1 $M_\odot$ and gas-to-dust mass ratios in the range ∼80–530 for our sources. However, these high gas-to-dust ratios are likely upper limits due to the continuum emission used to derive dust masses being optically thick.
3. There is good agreement between the line emission-based gas masses from this work and the ones measured from gas kinematics in the literature. With two exceptions, RXJ 1842.9-3532 and RXJ 1615.3-3255, the gas estimates from the two methods lie within a factor of ∼3 (1σ–2σ) of each other.
4. Gas disk masses from CO + N_2H^+ are on average a factor of $2.3^{+0.7}_{-1.0}\times$ lower than the kinematically measured gas masses. Assuming the kinematics trace the true disk mass, this could point toward slightly lower N_2

abundances and/or lower midplane ionization rates than typically assumed.

5. Herbig disks are found to have ISM-level CO gas abundances based on their CO and N_2H^+ fluxes, which sets them apart from T Tauri disks, where the CO abundance in the CO-emitting layer is typically $\sim$3–30$\times$ lower.

The agreement between the gas masses measured from gas kinematics and CO + N_2H^+ is promising as the former provides a direct estimate of the mass that does not depend on disk chemistry, whereas the latter is much more broadly applicable. It shows that multimolecule line fluxes are a robust tool to accurately measure disk masses at least for extended disks.

Acknowledgments

We would like to thank the anonymous referee for their insightful feedback. L.T. and K.Z. acknowledge the support of the NSF AAG grant #2205617. C.L. has received funding from the European Union's Horizon 2020 research and innovation program under the Marie Sklodowska-Curie grant agreement No. 823823 (DUSTBUSTERS) and by the UK Science and Technology research Council (STFC) via the consolidated grant ST/W000997/1. G.R. acknowledges funding from the Fondazione Cariplo, grant No. 2022-1217, and the European Research Council (ERC) under the European Union's Horizon Europe Research & Innovation Programme under grant agreement no. 101039651 (DiscEvol). Views and opinions expressed are, however, those of the author(s) only, and do not necessarily reflect those of the European Union or the European Research Council Executive Agency. Neither the European Union nor the granting authority can be held responsible for them. J.B. acknowledges support from NASA XRP grant No. 80NSSC23K1312. M.B., D.F., and J.S. have received funding from the European Research Council (ERC) under the European Union's Horizon 2020 research and innovation program (PROTOPLANETS, grant agreement No. 101002188). Computations have been done on the 'Mesocentre SIGAMM' machine, hosted by Observatoire de la Côte d'Azur. P.C. acknowledges support by the Italian Ministero dell'Istruzione, Università e Ricerca through the grant Progetti Premiali 2012 - iALMA (CUP C52I13000140001) and by the ANID BASAL project FB210003. S.F. is funded by the European Union (ERC, UNVEIL, 101076613). Views and opinions expressed are, however, those of the author(s) only and do not necessarily reflect those of the European Union or the European Research Council. Neither the European Union nor the granting authority can be held responsible for them. S. F. acknowledges financial contribution from PRIN-MUR 2022YP5ACE. M.F. is supported by a Grant-in-Aid from the Japan Society for the Promotion of Science (KAKENHI: No. JP22H01274). J.D.I. acknowledges support from an STFC Ernest Rutherford Fellowship (ST/W004119/1) and a University Academic Fellowship from the University of Leeds. Support for A.F.I. was provided by NASA through the NASA Hubble Fellowship grant No. HST-HF2-51532.001-A awarded by the Space Telescope Science Institute, which is operated by the Association of Universities for Research in Astronomy, Inc., for NASA, under contract NAS5-26555. G.L. acknowledges support from the European Union's Horizon 2020 research and innovation program under the Marie Sklodowska-Curie grant agreement #823823 (RISE DUSTBUSTERS project) and from the Italian MUR through PRIN 20228JPA3A. C.P. acknowledges Australian Research Council funding via FT170100040, DP18010423, DP220103767, and DP240103290. H.-W.Y. acknowledges support from National Science and Technology Council (NSTC) in Taiwan through grant NSTC 110-2628-M-001-003-MY3 and from the Academia Sinica Career Development Award (AS-CDA-111-M03). Support for B.Z. was provided by The Brinson Foundation. C.H. acknowledges support from the National Science Foundation Astronomy and Astrophysics Research grants program No. 2407679. A.J.W. has received funding from the European Union's Horizon 2020 research and innovation program under the Marie Skłodowska-Curie grant agreement No. 101104656.

This Letter makes use of the following ALMA data: ADS/JAO.ALMA#2023.1.00334.S, #2022.1.00485.S, #2021.1.01123.L, #2012.1.00158.S, #2012.1.00870.S, #2015.1.00192.S, #2015.1.00678.S, #2015.1.01017.S, #2016.1.00484.L, #2016.1.00724.S, #2017.1.00069.S, #2017.1.00940.S, #2017.1.01404.S, #2017.1.01419.S, #2018.1.00689.S, #2018.1.00945.S, #2018.1.01055.L, #2019.1.01683.S ALMA is a partnership of ESO (representing its member states), NSF (USA) and NINS (Japan), together with NRC (Canada), MOST and ASIAA (Taiwan), and KASI (Republic of Korea), in cooperation with the Republic of Chile. The Joint ALMA Observatory is operated by ESO, AUI/NRAO and NAOJ. The National Radio Astronomy Observatory is a facility of the National Science Foundation operated under cooperative agreement by Associated Universities, Inc.

All figures were generated with the `PYTHON`-based package `MATPLOTLIB` (J. D. Hunter 2007). This research made use of Astropy,[35] a community-developed core Python package for Astronomy (Astropy Collaboration et al. 2013, 2018).

Facilities: ALMA

Software: CASA (J. P. McMullin et al. 2007; CASA-Team et al. 2022), Astropy (Astropy Collaboration et al. 2013, 2018), MATPLOTLIB (J. D. Hunter 2007).

Appendix
Observational Details

This appendix contains Table A1, which provides information about the ALMA observations presented in this work. It also contains Table A2, which provides the integrated continuum and line fluxes used in this work.

[35] http://www.astropy.org

Table A1
ALMA Observation Details

Name	Date	ALMA Band 7—N_2H^+					
		Antennas	Baselines (m)	Time on Source (minutes)	Bandpass Calibrator	Phase Calibrator	Flux Calibrator
RXJ 1615.3-3255	2 Apr 2024	42	15–251	8	J1924-2914	J1626-2951	J1924-2914
	1 Jul 2024	41	15–1261	22	J1427-4206	J1427-4206	J1626-2951
	1 Jul 2024	36	15–649	23	J1427-4206	J1610-3958	J1427-4206
RXJ 1852.3-3700	1 Apr 2024	41	15–280	8	J1924-2914	J1839-3453	J1924-2914
	28 May 2024	42	15–984	23	J1924-2914	J1802-3940	J1924-2914
RXJ 1842.9-3532	1 Apr 2024	41	15–280	8	J1924-2914	J1839-3453	J1924-2914
	28 May 2024	42	15–984	23	J1924-2914	J1802-3940	J1924-2914
AA Tau	27 Jul 2024	46	14–499	9	J0423-0120	J0438+3004	J0423-0120
	8 Sep 2024	43	15–1604	25	J0423-0120	J0438+3004	J0423-0120
PDS 66	21 Mar 2024	45	15–313	9	J1427-4206	J1147-6753	J1427-4206
	29 May 2024	41	15–984	25	J1427-4206	J1147-6753	J1427-4206
HD 143006	12 Apr 2024	44	15–314	8	J1924-2914	J1625-2527	J1924-2914
	4 Jun 2024	40	15–1397	22	J1924-2914	J1551-1755	J1924-2914
HD 135344B	12 Apr 2024	44	15–313	8	J1924-2914	J1457-3539	J1924-2914
	28 May 2024	41	15–984	23	J1256-0547	J1457-3539	J1256-0547
CQ Tau	31 Jul 2024	45	14–483	9	J0423-0120	J0521+1638	J0423-0120
	22 Sep 2024	43	15–1397	25	J0423-0120	J0521+1638	J0423-0120
HD 34282	1 Aug 2024	46	14–313	23	J0423-0120	J0501-0159	J0423-0120
	1 Nov 2024	46	14–313	8	J0423-0120	J0501-0159	J0423-0120
MWC 758	31 Jul 2024	45	14–483	9	J0423-0120	J0521+1638	J0423-0120
	22 Sep 2024	43	15–1397	25	J0423-0120	J0521+1638	J0423-0120
Elias 2-27	6 Oct 2022	10	8–48	19	J1427-4206	J1625-2527	J1427-4206
	7 Oct 2022	10	8–48	34	J1427-4206	J1625-2527	J1427-4206
	9 Oct 2022	10	8–48	34	J1427-4206	J1625-2527	J1427-4206
	9 Jan 2023	40	15–740	28	J1427-4206	J1700-2610	J1427-4206
		ALMA Band 6—$C^{18}O$					
RXJ 1842.9-3532	21 Dec 2023	46	15–1397	32	J1924-2914	J1826-3650	J1924-2914
	25 Mar 2024	48	15–314	9	J1924-2914	J1826-3650	J1924-291

Table A2
ALMA Observations and Integrated Fluxes

Source	Disk-integrated Fluxes (mJy km s^{-1})				Program IDs	References
	285 GHz cont.	^{13}CO (2–1)	$C^{18}O$ (2–1)	N_2H^+ (3–2)		
DM Tau	99.1 ± 1.4	5341.7 ± 34.3	1275.6 ± 21.8	1437.6 ± 39.2	2016.1.00724.S, 2015.1.00678.S	(3, 2, 2, 3)
V4046 Sgr	576.0 ± 12.0	8275.7 ± 44.3	1936.0 ± 38.5	3736.1 ± 31.6	2016.1.00724.S, 2015.1.00678.S	(3, 2, 2, 3)
RXJ 1852.3-3700	93.0 ± 0.6	1587.5 ± 37.7	504.4 ± 22.1	541.0 ± 17.1	2018.1.00689.S, 2023.1.00334.S	(1, 1, 1, 1)
RXJ 1842.9[a]	87.6 ± 0.5	⋯	238 ± 4	359.4 ± 7.9	2023.1.00334.S, 2021.1.01123.L	(1, 4, 1, 1)
LkCa 15	281.0 ± 6.9	6074.2 ± 16.1	1198.1 ± 15.6	1869.0 ± 33.5	2018.1.00945.S, 2015.1.00678.S	(3, 5, 5, 3)
PDS 66	162.2 ± 8.0	790.0 ± 50.0	210.0 ± 20.0	1000.7 ± 14.5	2017.1.01419.S, 2023.1.00334.S	(1, 7, 7, 1)
CQ Tau	207.5 ± 1.9	1120.0 ± 40.0	600.0 ± 20.0	19.9 ± 5.88	2017.1.01404.S, 2023.1.00334.S	(1, 8, 8, 1)
HD 34282	205.2 ± 6.9	3460.0 ± 50.0	1890.0 ± 40.0	288.2 ± 9.2	2017.1.01404.S, 2023.1.00334.S	(1, 8, 8, 1)
MWC 758	101.3 ± 0.4	1870.0 ± 70.0	780.0 ± 40.0	71.8 ± 6.3	2017.1.00940.S, 2023.1.00334.S	(1, 8, 8, 1)
GM Aur	286.4 ± 2.6	5028.0 ± 48.0	1092.0 ± 39.0	1484.0 ± 14.6	2018.1.01055.L, 2015.1.00678.S	(3, 9, 9, 3)
AS 209	289.0 ± 4.5	2269.0 ± 38.0	538.0 ± 27.0	884.5 ± 14.3	2018.1.01055.L, 2015.1.00678.S	(3, 9, 9, 3)
IM Lup	243.7 ± 6.2	8370.0 ± 83.0	1592.0 ± 60.0	2040.0 ± 49.0	2018.1.01055.L, 2015.1.00678.S	(3, 9, 9, 3)
MWC 480	490.0 ± 49.0	8361.0 ± 57.0	3017.0 ± 41.0	228.0 ± 13.0	2018.1.01055.L, 2015.1.00657.S	(3, 9, 9, 10)
HD 163296	791.6 ± 1.6	15885.0 ± 80.0	5783.0 ± 51.0	556.1 ± 49.1	2018.1.01055.L, 2012.1.00681.S	(3, 9, 9, 11)
	285 GHz cont.	^{13}CO (3–2)	$C^{18}O$ (3–2)	N_2H^+ (3–2)		
RXJ 1615.3-3255	245.9 ± 0.4	11504.0 ± 41.8	3226.8 ± 48.2	563.6 ± 6.2	2012.1.00870.S, 2023.1.00334.S	(1, 1, 1, 1)
RXJ 1842.9-3532[a]	⋯	2831.2 ± 10.3	–		2023.1.00334.S, 2021.1.01123.L	(1, 4, 1, 1)
AA Tau	112.0 ± 0.5	5102.0 ± 42.0	1217.5 ± 53.4	686.6 ± 10.8	2015.1.01017.S, 2023.1.00334.S	(1, 7, 7, 1)
HD 143006	102.0 ± 0.4	1668.0 ± 7.6	483.3 ± 10.1	330.9 ± 8.8	2019.1.01683.S, 2023.1.00334.S	(1, 1, 1, 1)
HD 135344B	302.8 ± 0.6	7482.5 ± 39.1	3115.4 ± 46.1	40.3 ± 5.8	2012.1.00158.S, 2023.1.00334.S	(1, 12, 12, 1)
Elias 2-27	467.6 ± 0.5	22260.0 ± 90.0	4450.0 ± 60.0	447 ± 6.5	2016.1.00724.S, 2022.1.00485.S	(1, 13, 13, 1)

Notes.
[a] For RXJ 1842.9 the two CO isotopologue lines are ^{13}CO (3–2) from M. Galloway-Sprietsma et al. (2025) and $C^{18}O$ (2–1) from this work. Flux uncertainties do not include absolute flux uncertainties. References are given for each individual line.
References. 1: This work, 2: K. Flaherty et al. (2020), 3: C. Qi et al. (2019), 4: M. Galloway-Sprietsma et al. (2025), 5: J. A. Sturm et al. (2023), 6: R. A. Loomis et al. (2017), 7: Á. Ribas et al. (2023), 8: L. M. Stapper et al. (2024), 9: K. I. Oberg et al. (2021), 10: R. A. Loomis et al. (2020), 11: C. Qi et al. (2015), 12: N. van der Marel et al. (2016), 13: T. Paneque-Carreño et al. (2023).

ORCID iDs

Leon Trapman https://orcid.org/0000-0002-8623-9703
Cristiano Longarini https://orcid.org/0000-0003-4663-0318
Giovanni P. Rosotti https://orcid.org/0000-0003-4853-5736
Sean M. Andrews https://orcid.org/0000-0003-2253-2270
Jaehan Bae https://orcid.org/0000-0001-7258-770X
Marcelo Barraza-Alfaro https://orcid.org/0000-0001-6378-7873
Myriam Benisty https://orcid.org/0000-0002-7695-7605
Gianni Cataldi https://orcid.org/0000-0002-2700-9676
Pietro Curone https://orcid.org/0000-0003-2045-2154
Ian Czekala https://orcid.org/0000-0002-1483-8811
Stefano Facchini https://orcid.org/0000-0003-4689-2684
Daniele Fasano https://orcid.org/0000-0003-4679-4072
Mario Flock https://orcid.org/0000-0002-9298-3029
Misato Fukagawa https://orcid.org/0000-0003-1117-9213
Maria Galloway-Sprietsma https://orcid.org/0000-0002-5503-5476
Himanshi Garg https://orcid.org/0000-0002-5910-4598
Cassandra Hall https://orcid.org/0000-0002-8138-0425
Jane Huang https://orcid.org/0000-0001-6947-6072
John D. Ilee https://orcid.org/0000-0003-1008-1142
Andres F. Izquierdo https://orcid.org/0000-0001-8446-3026
Kazuhiro Kanagawa https://orcid.org/0000-0001-7235-2417
Geoffroy Lesur https://orcid.org/0000-0002-8896-9435
Giuseppe Lodato https://orcid.org/0000-0002-2357-7692
Ryan A. Loomis https://orcid.org/0000-0002-8932-1219
Ryuta Orihara https://orcid.org/0000-0003-4039-8933
Teresa Paneque-Carreno https://orcid.org/0000-0002-4044-8016
Christophe Pinte https://orcid.org/0000-0001-5907-5179
Daniel Price https://orcid.org/0000-0002-4716-4235
Jochen Stadler https://orcid.org/0000-0002-0491-143X
Richard Teague https://orcid.org/0000-0003-1534-5186
Sierk van Terwisga https://orcid.org/0000-0002-1284-5831
Leonardo Testi https://orcid.org/0000-0003-1859-3070
Hsi-Wei Yen https://orcid.org/0000-0003-1412-893X
Gaylor Wafflard-Fernandez https://orcid.org/0000-0002-3468-9577
David J. Wilner https://orcid.org/0000-0003-1526-7587
Andrew J. Winter https://orcid.org/0000-0002-7501-9801
Lisa Wölfer https://orcid.org/0000-0002-7212-2416
Tomohiro C. Yoshida https://orcid.org/0000-0001-8002-8473
Brianna Zawadzki https://orcid.org/0000-0001-9319-1296
Ke Zhang https://orcid.org/0000-0002-0661-7517

References

Acke, B., van den Ancker, M. E., & Dullemond, C. P. 2005, A&A, 436, 209
Agurto-Gangas, C., Pérez, L., Sierra, A., & Miley, J. M. 2025, ApJ, submitted
Aikawa, Y., Cataldi, G., Yamato, Y., et al. 2021, ApJS, 257, 13
Aikawa, Y., Umebayashi, T., Nakano, T., & Miyama, S. M. 1997, ApJL, 486, L51
Aikawa, Y., van Zadelhoff, G., van Dishoeck, E. F., & Herbst, E. 2002, A&A, 386, 622
Alcalá, J. M., Manara, C. F., France, K., et al. 2019, A&A, 629, A108
Alcalá, J. M., Manara, C. F., Natta, A., et al. 2017, A&A, 600, A20
Anderson, D. E., Blake, G. A., Bergin, E. A., et al. 2019, ApJ, 881, 127
Anderson, D. E., Cleeves, L. I., Blake, G. A., et al. 2022, ApJ, 927, 229
Anderson, D. E., Cleeves, L. I., Blake, G. A., et al. 2024, ApJ, 966, 84
Andrews, S. M., Teague, R., Wirth, C. P., Huang, J., & Zhu, Z. 2024, ApJ, 970, 153
Andrews, S. M., Terrell, M., Tripathi, A., et al. 2018a, ApJ, 865, 157
Andrews, S. M., Huang, J., Pérez, L. M., et al. 2018b, ApJL, 869, L41
Andrews, S. M., Wilner, D. J., Espaillat, C., et al. 2011, ApJ, 732, 42
Andrews, S. M., Wilner, D. J., Hughes, A. M., Qi, C., & Dullemond, C. P. 2009, AJ, 700, 1502
Ansdell, M., Williams, J. P., Trapman, L., et al. 2018, ApJ, 859, 21
Ansdell, M., Williams, J. P., van der Marel, N., et al. 2016, ApJ, 828, 46
Astropy Collaboration, Price-Whelan, A. M., Sipőcz, B. M., et al. 2018, AJ, 156, 123
Astropy Collaboration, Robitaille, T. P., Tollerud, E. J., et al. 2013, A&A, 558, A33
Barenfeld, S. A., Carpenter, J. M., Ricci, L., & Isella, A. 2016, ApJ, 827, 142
Beckwith, S. V. W., Sargent, A. I., Chini, R. S., & Guesten, R. 1990, AJ, 99, 924
Bergin, E. A., Cleeves, L. I., Gorti, U., et al. 2013, Natur, 493, 644
Bergin, E. A., Du, F., Cleeves, L. I., et al. 2016, ApJ, 831, 101
Bergin, E. A., Hogerheijde, M. R., Brinch, C., et al. 2010, A&A, 521, L33
Bergin, E. A., & Williams, J. P. 2018, Formation, Evolution, and Dynamics of Young Solar Systems, Astrophysics and Space Science Library, 445 (Cham: Springer)
Bergner, J. B., Öberg, K. I., Bergin, E. A., et al. 2019, ApJ, 876, 25
Birnstiel, T. 2024, ARA&A, 62, 157
Bosman, A. D., Walsh, C., & van Dishoeck, E. F. 2018, A&A, 618, A182
Bouvier, J., Chelli, A., Allain, S., et al. 1999, A&A, 349, 619
Bruderer, S. 2013, A&A, 559, A46
Bruderer, S., van Dishoeck, E. F., Doty, S. D., & Herczeg, G. J. 2012, A&A, 541, A91
Calahan, J. K., Bergin, E., Zhang, K., et al. 2021, ApJ, 908, 8
Carmona, A., van der Plas, G., van den Ancker, M. E., et al. 2011, A&A, 533, A39
CASA-Team, Bean, B., Bhatnagar, S., et al. 2022, PASP, 134, 114501
Cleeves, L. I., Bergin, E. A., Qi, C., Adams, F. C., & Öberg, K. I. 2015, ApJ, 799, 204
Curone, P., Facchini, S., Andrews, S. M., et al. 2025, ApJL 984, L9
Czekala, I., Loomis, R. A., Teague, R., et al. 2021, ApJS, 257, 2
D'Alessio, P., Cantö, J., Calvet, N., & Lizano, S. 1998, ApJ, 500, 411
Deng, D., Pascucci, I., & Vioque, M. 2025, ApJ, submitted
Dent, W. R. F., Greaves, J. S., & Coulson, I. M. 2005, MNRAS, 359, 663
Dionatos, O., Woitke, P., Güdel, M., et al. 2019, A&A, 625, A66
Drażkowska, J., Bitsch, B., Lambrechts, M., et al. 2023, in ASP Conf. Ser. 534, Protostars and Planets VII, ed. S. Inutsuka et al. (San Francisco, CA: ASP), 717
Dutrey, A., Guilloteau, S., Duvert, G., et al. 1996, A&A, 309, 493
Espaillat, C., D'Alessio, P., Hernández, J., et al. 2010, ApJ, 717, 441
Fairlamb, J. R., Oudmaijer, R. D., Mendigutía, I., Ilee, J. D., & van den Ancker, M. E. 2015, MNRAS, 453, 976
Flaherty, K., Hughes, A. M., Simon, J. B., et al. 2020, ApJ, 895, 109
Francis, L., & van der Marel, N. 2020, ApJ, 892, 111
Furuya, K., & Aikawa, Y. 2014, ApJ, 790, 97
Furuya, K., Lee, S., & Nomura, H. 2022, ApJ, 938, 29
Galloway-Sprietsma, M., Bae, J., Izquierdo, A., et al. 2025, ApJL, 984, L10
Guzmán-Díaz, J., Mendigutía, I., Montesinos, B., et al. 2021, A&A, 650, A182
Hendler, N., Pascucci, I., Pinilla, P., et al. 2020, ApJ, 895, 126
Herbig, G. H. 1960, ApJS, 4, 337
Herbig, G. H. 1977, ApJ, 214, 747
Herbig, G. H., & Bell, K. R. 1988, Third Catalog of Emission-Line Stars of the Orion Population, 3 (Santa Cruz, CA: Lick Observatory), 1111
Hildebrand, R. H. 1983, QJRAS, 24, 267
Hunter, J. D. 2007, CSE, 9, 90
Izquierdo, A. F., Stadler, J., Galloway-Sprietsma, M., et al. 2025, ApJL, 984, L8
Jorsater, S., & van Moorsel, G. A. 1995, AJ, 110, 2037
Kama, M., Bruderer, S., van Dishoeck, E. F., et al. 2016, A&A, 592, A83
Krijt, S., Bosman, A. D., Zhang, K., et al. 2020, ApJ, 899, 134
Krijt, S., Schwarz, K. R., Bergin, E. A., & Ciesla, F. J. 2018, ApJ, 864, 78
Kuznetsova, A., Bae, J., Hartmann, L., & Mac Low, M.-M. 2022, ApJ, 928, 92
Law, C. J., Crystian, S., Teague, R., et al. 2022, ApJ, 932, 114
Law, C. J., Teague, R., Loomis, R. A., et al. 2021, ApJS, 257, 4
Leemker, M., Booth, A. S., van Dishoeck, E. F., et al. 2022, A&A, 663, A23
Lodato, G., Rampinelli, L., Viscardi, E., et al. 2023, MNRAS, 518, 4481
Long, D. E., Cleeves, L. I., Adams, F. C., et al. 2024, ApJ, 972, 88
Long, F., Herczeg, G. J., Pascucci, I., et al. 2017, ApJ, 844, 99
Longarini, C., Lodato, G., Rosotti, G. P., et al. 2025, ApJL, 984, L17
Loomis, R., Facchini, S., Benisty, M., et al. 2025, ApJL, 984, L7
Loomis, R. A., Öberg, K. I., Andrews, S. M., & MacGregor, M. A. 2017, ApJ, 840, 23
Loomis, R. A., Öberg, K. I., Andrews, S. M., et al. 2020, ApJ, 893, 101
Luhman, K. L., & Mamajek, E. E. 2012, ApJ, 758, 31
Macías, E., Espaillat, C. C., Ribas, Á., et al. 2018, ApJ, 865, 37
Mamajek, E. E., Meyer, M. R., & Liebert, J. 2002, AJ, 124, 1670
Manara, C. F., Ansdell, M., Rosotti, G. P., et al. 2023, in ASP Conf. Ser. 534, Protostars and Planets VII, ed. S. Inutsuka et al. (San Francisco, CA: ASP), 539

Manara, C. F., Testi, L., Natta, A., et al. 2014, A&A, 568, A18
Martire, P., Longarini, C., Lodato, G., et al. 2024, A&A, 686, A9
McClure, M. K., Bergin, E. A., Cleevs, L. I., et al. 2016, ApJ, 831, 167
McMullin, J. P., Waters, B., Schiebel, D., Young, W., & Golap, K. 2007, in ASP Conf. Ser. 376, Astronomical Data Analysis Software and Systems XVI, ed. R. A. Shaw, F. Hill, & D. J. Bell (San Francisco, CA: ASP), 127
Miotello, A., Bruderer, S., & van Dishoeck, E. F. 2014, A&A, 572, A96
Miotello, A., Kamp, I., Birnstiel, T., Cleeves, L. C., & Kataoka, A. 2023, in ASP Conf. Ser. 534, Protostars and Planets VII, ed. S. Inutsuka et al. (San Francisco, CA: ASP), 501
Miotello, A., van Dishoeck, E., Williams, J., et al. 2017, A&A, 599, A113
Montesinos, B., Eiroa, C., Mora, A., & Merín, B. 2009, A&A, 495, 901
Morbidelli, A., & Raymond, S. N. 2016, JGRE, 121, 1962
Öberg, K. I., Facchini, S., & Anderson, D. E. 2023, ARA&A, 61, 287
Oberg, K. I., Guzman, V. V., Walsh, C., et al. 2021, ApJS, 257, 1
Paardekooper, S., Dong, R., Duffell, P., et al. 2023, in ASP Conf. Ser. 534, Protostars and Planets VII, ed. S. Inutsuka et al. (San Francisco, CA: ASP), 685
Paneque-Carreño, T., Miotello, A., van Dishoeck, E., Rosotti, G., & Tabone, B. 2025, arXiv:2501.08294
Paneque-Carreño, T., Miotello, A., van Dishoeck, E. F., et al. 2023, A&A, 669, A126
Paneque-Carreño, T., Pérez, L. M., Benisty, M., et al. 2021, ApJ, 914, 88
Pascucci, I., Herczeg, G., Carr, J., & Bruderer, S. 2013, AJ, 779, 178
Pérez, L. M., Carpenter, J. M., Andrews, S. M., et al. 2016, Sci, 353, 1519
Pérez, L. M., Chandler, C. J., Isella, A., et al. 2015, ApJ, 813, 41
Pinte, C., Ménard, F., Duchêne, G., et al. 2018, A&A, 609, A47
Pinte, C., Teague, R., Flaherty, K., et al. 2023, in ASP Conf. Ser. 534, Protostars and Planets VII, ed. S. Inutsuka et al. (San Francisco, CA: ASP), 645
Powell, D., Gao, P., Murray-Clay, R., & Zhang, X. 2022, NatAs, 6, 1147
Qi, C., Öberg, K. I., Andrews, S. M., et al. 2015, ApJ, 813, 128
Qi, C., Öberg, K. I., Espaillat, C. C., et al. 2019, ApJ, 882, 160
Qi, C., Öberg, K. I., Wilner, D. J., et al. 2013, Sci, 341, 630
Qi, C., & Wilner, D. J. 2024, ApJ, 977, 60
Quast, G. R., Torres, C. A. O., de La Reza, R., da Silva, L., & Mayor, M. 2000, in IAU Symp. 200, ed. B. Reipurth & H. Zinnecker (Cambridge: Cambridge Univ. Press), 28
Ribas, Á., Macías, E., Weber, P., et al. 2023, A&A, 673, A77
Rosotti, G., Longarini, C., Paneque-Carreno, T., et al. 2025, ApJL, 984, L20
Ruaud, M., & Gorti, U. 2019, ApJ, 885, 146
Ruaud, M., Gorti, U., & Hollenbach, D. J. 2022, ApJ, 925, 49
Schwarz, K. R., Bergin, E. A., Cleeves, L. I., et al. 2018, ApJ, 856, 85
Schwarz, K. R., Calahan, J. K., Zhang, K., et al. 2021, ApJS, 257, 20
Seifert, R. A., Cleeves, L. I., Adams, F. C., & Li, Z.-Y. 2021, ApJ, 912, 136
Sierra, A., Pérez, L. M., Zhang, K., et al. 2021, ApJS, 257, 14
Stadler, J., Benisty, M., Winter, A. J., et al. 2025, ApJL, 984, L11
Stapper, L. M., Hogerheijde, M. R., van Dishoeck, E. F., et al. 2024, A&A, 682, A149
Sturm, J. A., Booth, A. S., McClure, M. K., Leemker, M., & van Dishoeck, E. F. 2023, A&A, 670, A12
Tazzari, M., Testi, L., Natta, A., et al. 2021, MNRAS, 506, 5117
Teague, R. 2020, richteague/keplerian_mask: Initial Release, v1.0, Zenodo, doi:10.5281/zenodo.4321137
Teague, R., Benisty, M., Facchini, S., et al. 2025, ApJL, 984, L6
Thi, W. F., van Dishoeck, E. F., Blake, G. A., et al. 2001, ApJ, 561, 1074
Trapman, L., Miotello, A., Kama, M., van Dishoeck, E. F., & Bruderer, S. 2017, A&A, 605, A69
Trapman, L., Tabone, B., Rosotti, G., & Zhang, K. 2022a, ApJ, 926, 61
Trapman, L., Zhang, K., Rosotti, G., et al. 2025, ApJ, submitted
Trapman, L., Zhang, K., van't Hoff, M. L. R., Hogerheijde, M. R., & Bergin, E. A. 2022b, ApJL, 926, L2
Tripathi, A., Andrews, S. M., Birnstiel, T., & Wilner, D. J. 2017, ApJ, 845, 44
Van Clepper, E., Bergner, J. B., Bosman, A. D., Bergin, E., & Ciesla, F. J. 2022, ApJ, 927, 206
van der Marel, N., van Dishoeck, E. F., Bruderer, S., et al. 2016, A&A, 585, A58
van't Hoff, M. L. R., Harsono, D., Tobin, J. J., et al. 2020, ApJ, 901, 166
van 't Hoff, M. L. R., Tobin, J. J., Harsono, D., & van Dishoeck, E. F. 2018, A&A, 615, A83
van 't Hoff, M. L. R., Walsh, C., Kama, M., Facchini, S., & van Dishoeck, E. F. 2017, A&A, 599, A101
Veronesi, B., Longarini, C., Lodato, G., et al. 2024, A&A, 688, A136
Veronesi, B., Paneque-Carreño, T., Lodato, G., et al. 2021, ApJL, 914, L27
Visser, R., van Dishoeck, E. F., & Black, J. H. 2009, A&A, 503, 323
Whitney, B. A., Robitaille, T. P., Bjorkman, J. E., et al. 2013, ApJS, 207, 30
Williams, J. P., Andrews, S. M., & Wilner, D. J. 2005, ApJ, 634, 495
Williams, J. P., & Best, W. M. J. 2014, ApJ, 788, 59
Yu, M., Evans, N. J. I., Dodson-Robinson, S. E., Willacy, K., & Turner, N. J. 2017, ApJ, 841, 39
Yu, M., Willacy, K., Dodson-Robinson, S. E., Turner, N. J., & Evans, N. J. I. 2016, ApJ, 822, 53
Zhang, K., Booth, A. S., Law, C. J., et al. 2021, ApJS, 257, 5
Zhang, K., Pérez, L., Pascucci, I., et al. 2025, ApJ, submitted